



Pushing the boundaries  
of chemistry?  
It takes  
#HumanChemistry

Make your curiosity and talent as a chemist matter to the world with a specialty chemicals leader. Together, we combine cutting-edge science with engineering expertise to create solutions that answer real-world problems. Find out how our approach to technology creates more opportunities for growth, and see what chemistry can do for you at:

[evonik.com/career](https://www.evonik.com/career)



# Recent Advances on Dual-Band Electrochromic Materials and Devices

Yanling Zhai, Jiahui Li, Sophia Shen, Zhijun Zhu,\* Sui Mao, Xiao Xiao, Chengzhou Zhu, Jianguo Tang, Xiaoquan Lu,\* and Jun Chen\*

Dual-band electrochromism is a phenomenon where materials can independently regulate the transmittance of visible (VIS) and near-infrared (NIR) light. Owing to their bistability, low energy consumption, and independent control over VIS and NIR regions, dual-band electrochromic (EC) devices have been of great significance to fully harnessing VIS and NIR light and building an energy-saving society. The past several years have witnessed the efforts put in developing novel EC materials to improve their dual-band optical performance through altering their composition, structural, and physicochemical features, which determine the optical behavior of dual-band EC devices. In this review, the concept, significance, working principle, and key influence factors of dual-band electrochromism are briefly introduced. Next, the up-to-date progress of dual-band EC materials including inorganic, organic, and composites materials are summarized, with a focus on material design, device fabrication, and performance optimization. Finally, the challenges and perspectives of dual-band EC materials and devices are also presented.

## 1. Introduction

Electrochromic (EC) materials and devices are capable of reversibly regulating their optical properties via redox reactions with applied bias voltages.<sup>[1–2]</sup> Since its first report in 1961,<sup>[3]</sup> EC technology has received enormous attention and has been rapidly developed over the past several decades.<sup>[4–14]</sup> With a collection of compelling features, including bistability, low energy consumption, and a fast process, electrochromism has exhibited great commercial potential in applications such as smart windows, low-energy displays, and energy-saving glass.<sup>[15–17]</sup> Currently, most EC materials focus on the regulation of visible (VIS) light.<sup>[18–20]</sup> However, nearly 50% of solar energy is located in the near infrared (NIR) region (780–2500 nm, **Figure 1a**),<sup>[21,22]</sup> which can pass through glass panels and significantly raise indoor temperatures but has not yet been well

controlled in traditional EC devices.<sup>[15]</sup> Consequently, about 41% of global energy consumption is used to maintain a comfortable light and temperature environment inside buildings,<sup>[23]</sup> arousing extensive concerns about the thermal regulation of NIR irradiation. Therefore, the development of EC materials capable of independently controlling both VIS and NIR transmittance (referred to as “dual-band” electrochromism) in accordance with weather conditions and personal preferences is of great significance to separately regulate the light and heat entering buildings.<sup>[24]</sup> Four EC modes of “bright”, “dark”, “warm”, and “cool” (illustrated in **Figure 1b**) are expected to be achieved using dual-band EC materials in smart windows. These smart windows would contribute to reducing the global energy consumption across building heating and cooling systems by blocking undesired NIR light in summer and intelligently allowing its passage in winter.<sup>[25]</sup>


EC materials, whose optical properties determine the EC performance of the device, are the key components in developing dual-band smart EC systems. Great efforts have been devoted to designing and synthesizing various materials with excellent dual-band EC performance, such as separate potential ranges over VIS and NIR regions, fast switching speed, and excellent cycle stability, to promote the further development and commercialization of dual-band EC devices.<sup>[26–30]</sup> There have been some excellent review articles regarding the synthesis and

Y. Zhai, J. Li, Z. Zhu, S. Mao, J. Tang, X. Lu  
Institute of Molecular Metrology  
College of Chemistry and Chemical Engineering  
Institute of Hybrid Materials  
College of Materials Science and Engineering  
Qingdao University  
Qingdao 266071, P. R. China  
E-mail: zhuzhijun@qdu.edu.cn; xiaoquanlu@qdu.edu.cn

S. Shen, X. Xiao, J. Chen  
Department of Bioengineering  
University of California, Los Angeles  
Los Angeles, CA 90095, USA  
E-mail: jun.chen@ucla.edu

C. Zhu  
College of Chemistry  
Central China Normal University  
Wuhan 430079, P. R. China

X. Lu  
Key Laboratory of Bioelectrochemistry and Environmental Analysis  
of Gansu Province  
College of Chemistry and Chemical Engineering  
Northwest Normal University  
Lanzhou 730070, China

 The ORCID identification number(s) for the author(s) of this article can be found under <https://doi.org/10.1002/adfm.202109848>.

DOI: 10.1002/adfm.202109848

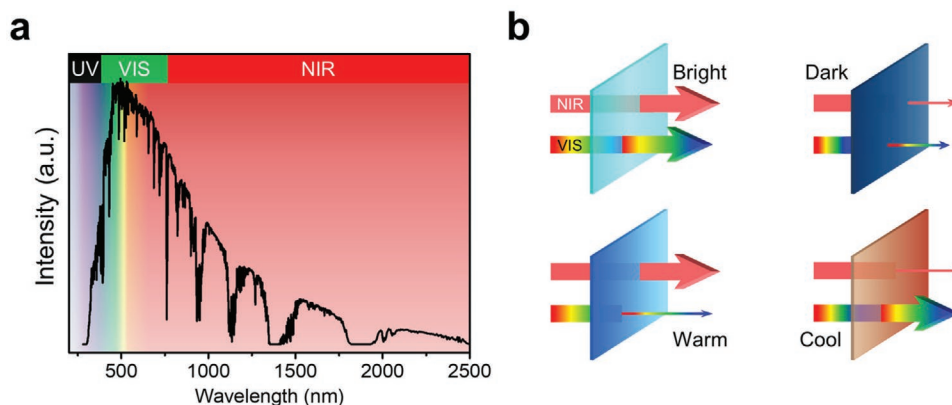
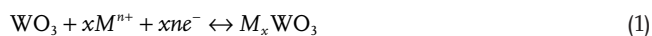


**Figure 1.** a) The solar spectrum and its energy distribution. The spectrum data were obtained from <https://www.pveducation.org/pvc/drom/appendices/standard-solar-spectra>. b) Illustration of the four distinct dual-band EC modes. Reproduced with permission.<sup>[127]</sup> Copyright 2020, American Chemical Society.

application of EC materials,<sup>[22,31–39]</sup> however, few have paid special attention to smart dual-band EC materials.<sup>[40]</sup> Inspired by the urgent need and increasing efforts in synthesizing high-performance dual-band EC materials,<sup>[27–28,41–43]</sup> this review will systematically discuss the latest development of dual-band EC materials and devices according to their material composition: inorganic, organic, and hybrid composite. The comparisons of key parameters among various EC materials are also presented to demonstrate the respective features of each individual material, which will inspire further research in the optimization of dual-band EC devices. Finally, the review will conclude with a discussion of the challenges and perspectives for future research on dual-band EC materials and devices.

## 2. Inorganic EC Materials

Inorganic materials such as metal oxide semiconductors and inorganic-inorganic composites have attracted extensive attention due to their high optical contrast, good cycle stability, and excellent durability.<sup>[44–45]</sup> It has been well-accepted that the EC behavior of metal oxides originates from the double injection and extraction of cations and electrons simultaneously upon various potentials.<sup>[46]</sup> For example,  $\text{WO}_3$  is an EC material that has been extensively investigated, and the reversible EC processes of  $\text{WO}_3$  can be expressed with the following reaction:<sup>[47–48]</sup>



where  $\text{M}^{n+}$  can be  $\text{H}^+$ ,  $\text{Li}^+$ ,  $\text{Na}^+$ ,  $\text{K}^+$ ,  $\text{Zn}^{2+}$ ,  $\text{Al}^{3+}$ , etc.,  $e^-$  represents an electron, and  $x$  is the stoichiometric coefficient, varying between 0 and 1. When a negative voltage is applied,  $\text{WO}_3$  film appears blue in color, accompanied by a double injection of cations and electrons. When the cations and electrons are extracted under a positive voltage, the film transits into a bleached state, appearing transparent.<sup>[49]</sup> The intercalation and extraction of  $\text{M}^{n+}$  are generally limited to a very thin surface layer of the EC material, which strongly depends on its microstructure.<sup>[50]</sup> Thus, optimizing the microstructure of the materials is critical to improving their EC performance, as it will provide more active

sites and increase the accessible intercalation sites, leading to a fast switching speed and high optical contrast.<sup>[51]</sup> Cai et al. fabricated three kinds of vertically aligned  $\text{WO}_3$  nanocluster, nanotree, and nanowire arrays, respectively, on fluorine-doped tin oxide (FTO) substrates by changing the amount of HCl during the synthesis process. Compared with the nanocluster,  $\text{WO}_3$  nanotree and nanowire arrays revealed faster switching speed, higher coloration efficiency, larger optical contrast, and improved cycling durability. These improvements can be attributed to the faster  $\text{H}^+$  diffusion rate and more efficient charge transfer mainly originating from the unique nanostructure and larger porous network of the vertically aligned nanotree and nanowire.<sup>[50]</sup> Additionally, the particle size of EC materials is also crucial to their EC performance.<sup>[52]</sup> Most recently, Yao et al. constructed EC films composed of  $\text{WO}_3$  quantum dots (QDs) with a hexagonal crystal structure and an average diameter of 1.2 nm. The ultrasmall size and the clear surface of  $\text{WO}_3$  QDs can provide high surface accessibility, shorten the diffusion path of the intercalation cations,<sup>[44]</sup> and increase the contact interface between cations and the electrode materials, which is critical to improve EC performance.<sup>[53]</sup> In addition to the diffusion-controlled intercalation of the  $\text{M}^{n+}$ ,  $\text{WO}_3$  also exhibits (pseudo) capacitive charge storage-induced EC behavior, which is associated with  $\text{M}^{n+}$  adsorption on the surface. These two competing processes are highly dependent on the structural and morphological characteristics of  $\text{WO}_3$ .<sup>[29]</sup>

Metal oxide semiconductors always possess free carrier densities in the range of  $\approx 10^{21} \text{ cm}^{-3}$ , leading to pronounced absorption in NIR and mid-IR regions.<sup>[54]</sup> The absorption bands of metal oxide nanocrystals (NCs) can be effectively managed by tuning their localized surface plasmon resonance (LSPR) via either aliovalent atom-doping or electrochemical doping at sufficient potentials.<sup>[54–56]</sup> LSPR is a phenomenon in which light absorption can be enhanced when the incident light frequency matches the natural resonance frequency of collective electron oscillations of the materials,<sup>[22,57–60]</sup> and the LSPR frequency is positively correlated with the free carrier density.<sup>[61–62]</sup> LSPR occurs not only on the surface of plasmonic metals such as Au and Ag, but also in metal oxide semiconductors with extraordinary free carrier densities.<sup>[58,61]</sup> Conventional plasmonic Au and Ag nanoparticles (NPs) have large

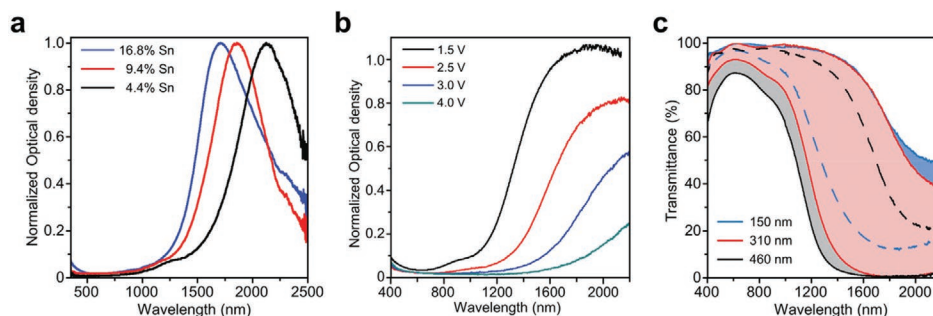


**Figure 2.** Optical spectra of ITO NCs. a) Normalized absorption spectra of ITO NCs with various tin-doping contents. b) Absorption spectra of the film composed of ITO NCs (16.8% Sn doping) with a diameter of 4.1 nm. c) Transmission spectra of ITO NCs (4.5 nm, 16.8% Sn doping) at bleached (1.5 V, versus  $\text{Li}^+/\text{Li}$ ) and colored (4 V) states for various film thicknesses. Reproduced with permission.<sup>[63]</sup> Copyright 2011, American Chemical Society.

free electron densities, so their LSPR frequency is usually not adjustable and the LSPR bands are always located in the VIS region. On the other hand, the free carrier densities of metal oxide semiconductor NCs are about one to two orders of magnitude lower than those of the plasmonic metal NPs. This allows for much easier modification of the LSPR frequency by varying the doping type and content, leading to an LSPR in the NIR or mid-IR regions.<sup>[62]</sup> In 2011, Milliron et al. reported a tin-doped indium oxide (ITO) NC film with tunable optical transmittance in the NIR range, whose LSPR peak is highly dependent on various Sn doping levels and thus the electron density of ITO (**Figure 2a**). The EC films fabricated from ITO NCs with 16.8% Sn showed controllable NIR absorption intensities under various voltages and high NIR contrast in both the colored and bleached states (**Figure 2b,c**).<sup>[63]</sup>

Considering the respective VIS and NIR light modulation abilities of different materials, it is possible to blend the materials of complementary EC properties to form nanocomposites for dual-band EC modulation.<sup>[46,64]</sup> In a pioneering study, Milliron et al. proposed a dual-band EC system by introducing ITO NCs into niobium oxide ( $\text{NbO}_x$ ). ITO NCs are able to tune NIR light in the potential range between 4 and 2.3 V (versus  $\text{Li}^+/\text{Li}$ ), while pure  $\text{NbO}_x$  can modulate VIS transmittance in a separate potential range of 2.3–1.5 V. Remarkably, the VIS optical contrast of the ITO- $\text{NbO}_x$  composites was five times higher than that of pure  $\text{NbO}_x$  in VIS region. This demonstrates the successful fabrication of a composite dual-band EC system with much better performance than individual materials.<sup>[65]</sup>

On the other hand, recent studies have also shown that surface capacitive charging/discharging upon cation adsorption/desorption can also change the free carrier density of the metal oxide semiconductor and thus strongly affect LSPR modulation.<sup>[66–67]</sup> Considering the aforementioned VIS-modulating function resulting from cation intercalation/deintercalation, single component heteroatom doped metal oxide semiconductors are expected to work as dual-band EC materials as the cation adsorption and intercalation take place under different potentials. Therefore, great effort has been put into developing novel inorganic materials capable of independently regulating VIS and NIR transmittance. This section will provide a discussion on the inorganic dual-band EC materials including  $\text{WO}_3$ - and  $\text{TiO}_2$ - and other metal oxide-based materials/composites.

## 2.1. $\text{WO}_3$ -Based Dual-Band Materials

$\text{WO}_3$  is a broad family of polymorphic compounds with inherent tunnels and excellent ion-hosting capacity. The solar light passing through  $\text{WO}_3$  can be regulated in amplitude and energy due to the adjustable bandgap by varying the crystalline structure and oxygen stoichiometry.<sup>[68–73]</sup> As shown in **Figure 3a**, when the oxygen vacancies in  $\text{WO}_3$  NPs increased from  $\text{WO}_3$  to  $\text{WO}_{2.92}$ ,  $\text{WO}_{2.83}$ ,  $\text{WO}_{2.72}$ , and  $\text{WO}_2$ , transmittance in the VIS region decreased along with a blue-shift of the absorption peak.<sup>[74]</sup> This is in accordance with a later report

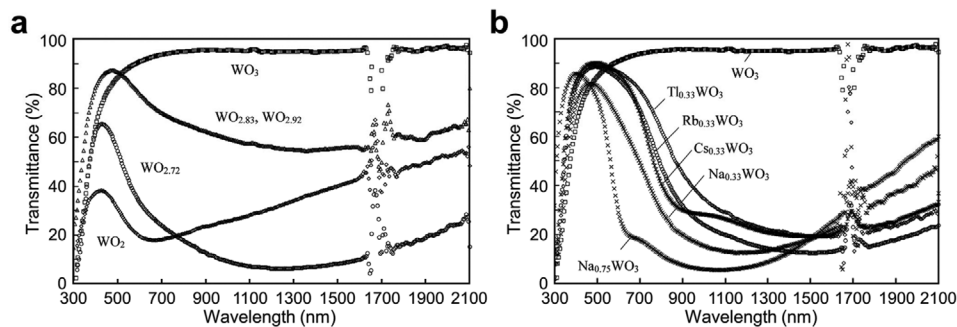


**Figure 3.** Optical spectra of  $\text{WO}_3$ -based materials. Transmittance spectra of a) tungsten oxide NPs with various oxygen vacancies and b) different types of  $\text{M}_x\text{WO}_3$  NPs dispersed in toluene (0.01 wt%). The disturbance between 1620 and 1790 nm is due to the absorption of toluene. Reproduced with permission.<sup>[74]</sup> Copyright 2007, American Ceramic Society.

which discovered that the introduction of oxygen into  $\text{WO}_{3-x}$  lattice upon being heated in air led to decreased LSPR absorption in the NIR region by reducing the charge carrier density.<sup>[75]</sup> In addition, the type and concentration of the injection cations have a significant effect on the transmittance spectra of  $\text{M}_x\text{WO}_3$  (Figure 3b),<sup>[74]</sup> which provides a wide range of possibilities for the optical modulation of  $\text{WO}_3$ . With advantages such as multiple oxidation states, high coloration efficiency, large optical regulation range, and good chemical stability,<sup>[45,76]</sup>  $\text{WO}_3$ -based dual-band EC devices have attracted great interest.<sup>[36,77]</sup>

### 2.1.1. Multi-Component EC Materials

Currently, most metal oxides are capable of blocking either the VIS or NIR region of solar light, which opens up avenues of fabricating dual-band EC materials by forming composite materials with complementary EC behaviors.<sup>[46]</sup>  $\text{WO}_{3-x}$  NCs have been known for their ability to selectively modulate NIR light by tuning their LSPR property upon alternant voltages.<sup>[78]</sup> To complement the NIR response of the  $\text{WO}_{3-x}$  NCs, Milliron et al. chose a VIS-modulating component, amorphous  $\text{NbO}_x$ , to fabricate a dual-band EC device.<sup>[64]</sup> To promote the EC performance of the  $\text{WO}_{3-x}$ - $\text{NbO}_x$  composite,  $\text{WO}_{3-x}$  NCs were assembled into a mesoporous architecture (Figure 4a), using a block copolymer as a sacrificial template, to form an open network which was subsequently filled with  $\text{NbO}_x$  (Figure 4b). The mesoporous film allows fast infiltration of the electrolyte for contact with both  $\text{WO}_{3-x}$  and  $\text{NbO}_x$ , resulting in faster color switching and higher optical contrast compared with a compact one. The composite film was transparent in both NIR and VIS regions at 4 V (versus  $\text{Li}^+/\text{Li}$ , bright mode) because both  $\text{WO}_{3-x}$  and  $\text{NbO}_x$  were fully discharged. At 2.3 V,  $\text{WO}_{3-x}$  NCs are selectively

charged, giving rise to improved LSPR absorption in the NIR region. Then, at 1.5 V,  $\text{NbO}_x$  is reduced by  $\text{Li}^+$  ion intercalation, which induces VIS polaronic absorption of the composite film, resulting in the dark mode (Figure 4c). Moreover, only 5.7% of the charge capacity of the composite film was lost after 2000 cycles, much lower than those of single component  $\text{WO}_{3-x}$  (21%) and  $\text{NbO}_x$  (11%) films (Figure 4d), which was ascribed to the robust architecture of the composite film.

Dual-band EC composites often require deliberate design of the porous structure to improve the mass transport of electrolytes into a deep region of the EC-active components. Making external channels through the template method is workable but laborious, so instead intrinsic tunnels within EC materials can be directly utilized to provide extra EC material-electrolyte interfaces. Prussian blue (PB) NCs are known for their VIS light modulation,<sup>[17]</sup> which features an open framework structure with a tunnel size of 3.2 Å to allow the passage of insertion ions.<sup>[79–80]</sup> Recently, Zhao et al. designed a dual-band EC device via electrodeposition of PB film onto  $\text{W}_{18}\text{O}_{49}$  nanowires (NWs) substrates.<sup>[46]</sup> The PB overcoat layer containing an intrinsic tunnel structure allows the efficient permeation of electrolytes to be in contact with the inner  $\text{W}_{18}\text{O}_{49}$  NWs layer (Figure 5a). Notably, this layer shows a slight increase in the switching time of  $\text{W}_{18}\text{O}_{49}$  NWs (Figure 5b), indicating its excellent  $\text{Li}^+$ -permeation nature. The optimized  $\text{W}_{18}\text{O}_{49}$  NWs/PB composites can successfully deliver the four distinct EC modes at different potentials (Figure 5c). Furthermore, the transmittance modulation contrast of the  $\text{W}_{18}\text{O}_{49}$ /PB composites is about 71.2% and 64.8% before and 70% and 58% after 100 repeated cycles at 633 and 1600 nm, respectively (Figure 5d), revealing the high-coloration contrast and the comparable cycle stability of the  $\text{W}_{18}\text{O}_{49}$  NWs/PB composite electrode in both the VIS and NIR regions. This work demonstrates that the intrinsic intracrystalline

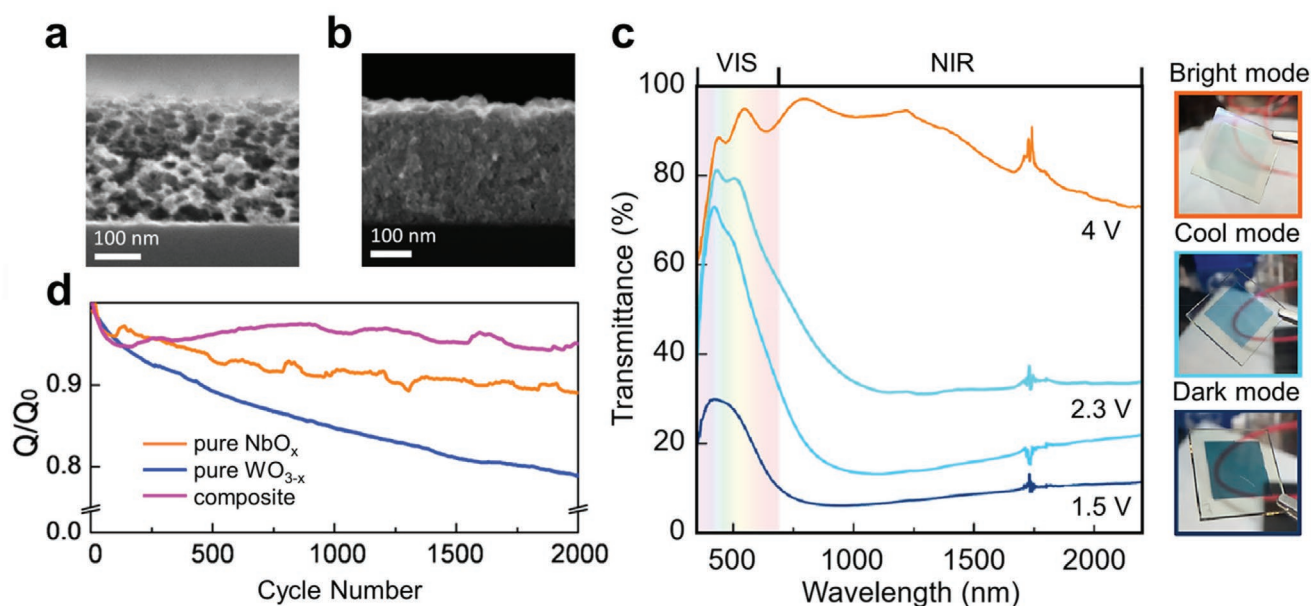


**Figure 4.** Structure, optical, and charge capacity profiles of  $\text{WO}_3$ -based films. Cross-section SEM images of  $\text{WO}_{3-x}$  a) and  $\text{WO}_{3-x}$ - $\text{NbO}_x$  composite b) films. c) Transmittance spectra of the composite film at indicated voltages (versus  $\text{Li}^+/\text{Li}$ ), and the corresponding photographs of the sample. d) Normalized charge capacity profiles of three films over 2000 cycles. Reproduced with permission.<sup>[64]</sup> Copyright 2015, American Chemical Society.

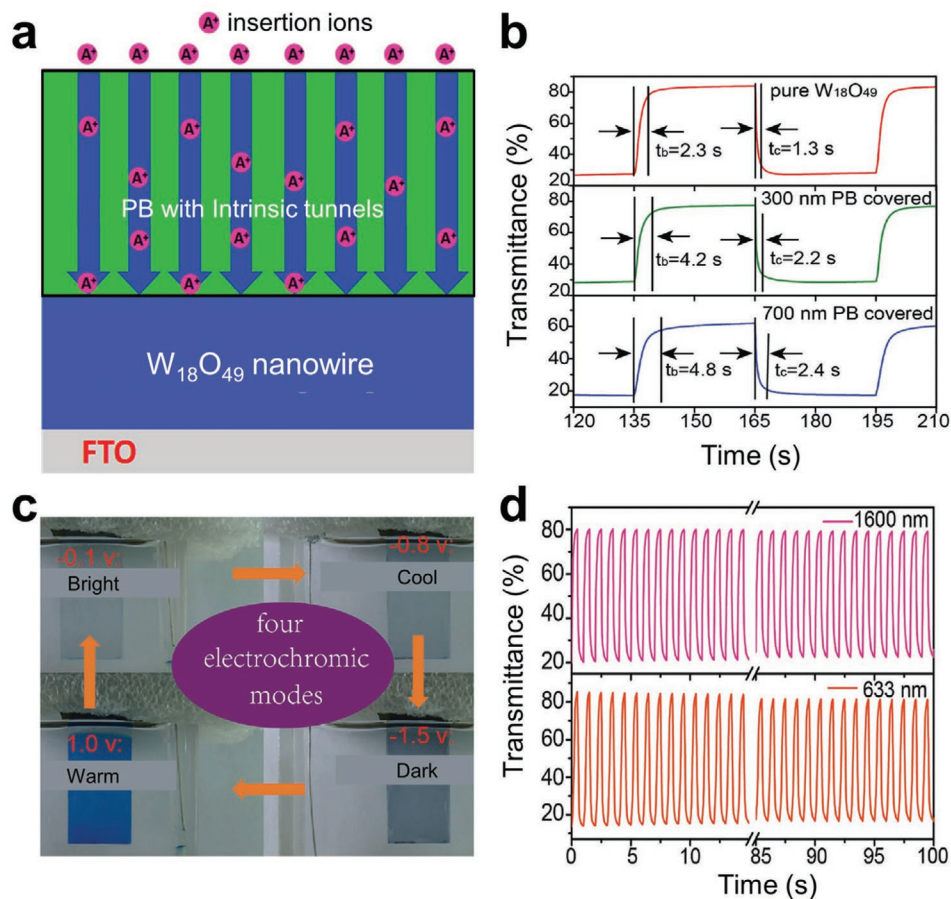


**Figure 5.** Structure and EC performance of  $W_{18}O_{49}$ -PB films. a) Illustration of  $W_{18}O_{49}$  NWs layers with PB overcoat layer. b) The transmittance-time profiles of  $W_{18}O_{49}$  NWs with and without PB overcoat layers with different thicknesses at 633 nm. c) The photographs of  $W_{18}O_{49}$ -PB film at indicated voltages (versus AgCl/Ag). d) The transmittance at 1600 and 633 nm at switching voltages. Reproduced with permission.<sup>[46]</sup> Copyright 2017, Wiley-VCH.

tunnel structure could be employed to construct high-performance dual-band EC devices by improving the penetration of insertion ions for contact with inner EC components.

To simplify the fabrication process and improve the performance of dual-band EC devices, Liu et al. proposed a simple and universal method to integrate VIS- and NIR-active components,  $W_{18}O_{49}$  NWs and  $K_{28}Li_5H_7P_8W_{48}O_{184} \cdot 92H_2O$  ( $P_8W_{48}$ ), respectively, into one dual-band EC device through a layer-by-layer (LBL) assembling technology.<sup>[23]</sup>  $W_{18}O_{49}$  NWs worked as NIR absorption materials because of their unique LSPR absorption caused by O-vacancies and high carrier density as the voltage decreased from 0.4 to  $-1.0$  V (versus AgCl/Ag) (Figure 6a).<sup>[75,81–82]</sup> On the other hand, the reduced form of  $P_8W_{48}$  exhibited strong absorption of VIS light from  $-0.6$  to  $-1.0$  V (Figure 6b). As a result, the  $W_{18}O_{49}/P_8W_{48}$  composite film was able to reversibly switch between three optical states—bright, cool, and dark modes—by varying voltage (Figure 6c). Furthermore, the composite film showed excellent electrochemical stability, with only 2.4% and 3.2% decay at 500 (Figure 6d) and 1060 nm (Figure 6e), respectively, after 500 cycles. No power density change was observed after being repeated more than 100 times (Figure 6f). These results demonstrate the excellent stability of the composite film, which was

ascribed to the stable nature of both components as well as precise control of the structure. Thus, a dual-band EC window with quick response, high efficiency, and durability was successfully fabricated from the arrangement of  $W_{18}O_{49}$  and  $P_8W_{48}$  through a facile LBL method.

The effect of anode materials has long been neglected as most of the effort in developing dual-band EC devices is focused on cathode ones. It is desirable for anode materials to maintain full transparency during the EC process and their charge-balancing function when they pair with the cathode materials. ITO NCs with suitable Sn doping show much greater ion storage capacity when compared with commercial ITO glass because of the dense and thin ITO coating layer on glass, which does not have enough area. Most recently, Lee et al.<sup>[26]</sup> reported a dual-band EC device using  $WO_{3-x}$  NWs and ITO NCs as an EC cathode and high-performance charge-balancing anode, respectively. The ITO NCs with 2% Sn doping were chosen after evaluating the trade-off between the NIR transparency and electrical conductivity, and their small size and relatively high surface area could accelerate the optical response by acting as an ion storage layer and guaranteeing the fast ion adsorption/desorption. As shown in Figure 7a, the  $WO_{3-x}$  NW film cathode exhibited a contrast of 42.5% and 68.8% at 633 and 1200 nm under  $-2.8$  V

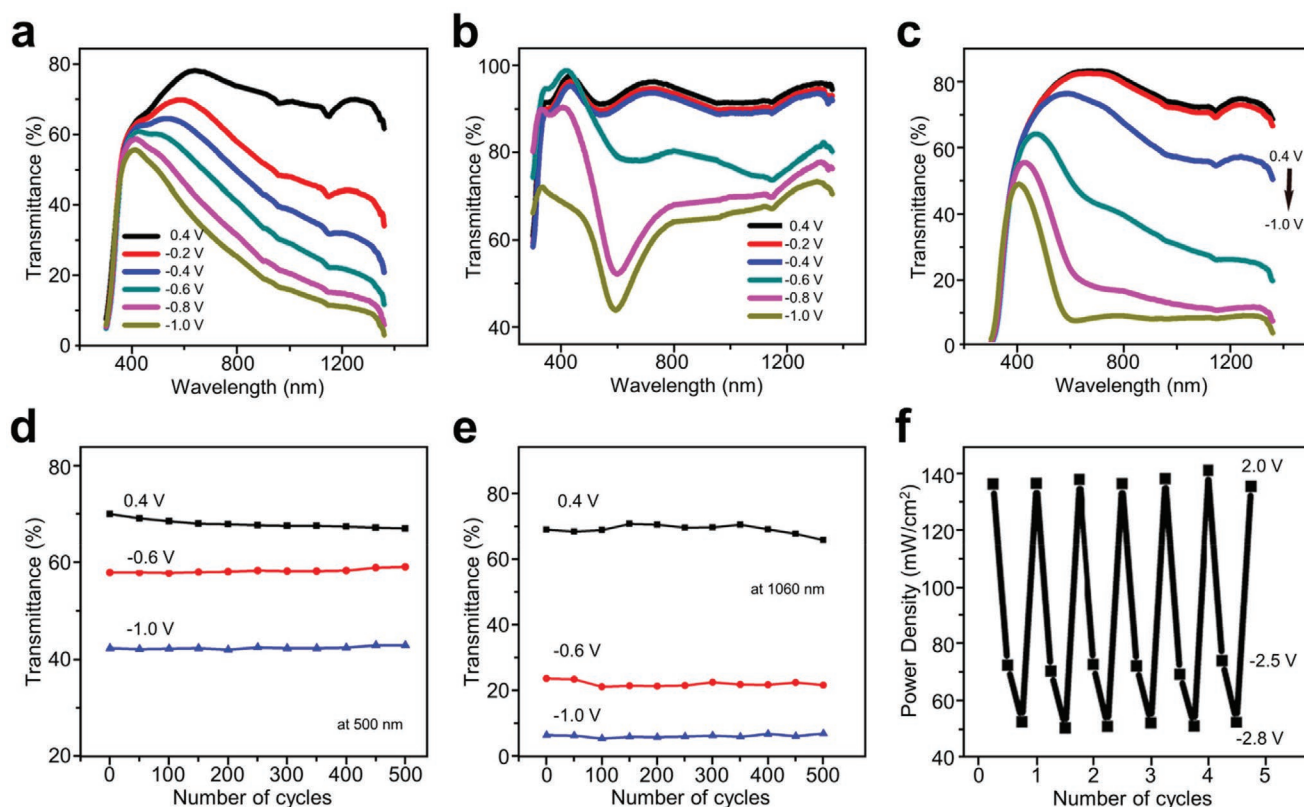


**Figure 6.** Transmission and power density profiles of  $W_{18}O_{49}/P_8W_{48}$  film. Transmission spectra of a)  $W_{18}O_{49}$ , b)  $P_8W_{48}$ , and c)  $W_{18}O_{49}/P_8W_{48}$  films at indicated voltages. Cycle performance of  $W_{18}O_{49}/P_8W_{48}$  film at d) 500 nm and e) 1060 nm for 500 cycles. f) Power density change of the transmitted light through  $W_{18}O_{49}/P_8W_{48}$  smart window by varying the applied voltage. All voltages used in this caption are quoted with respect to an AgCl/Ag reference. Reproduced with permission.<sup>[23]</sup> Copyright 2018, American Chemical Society.

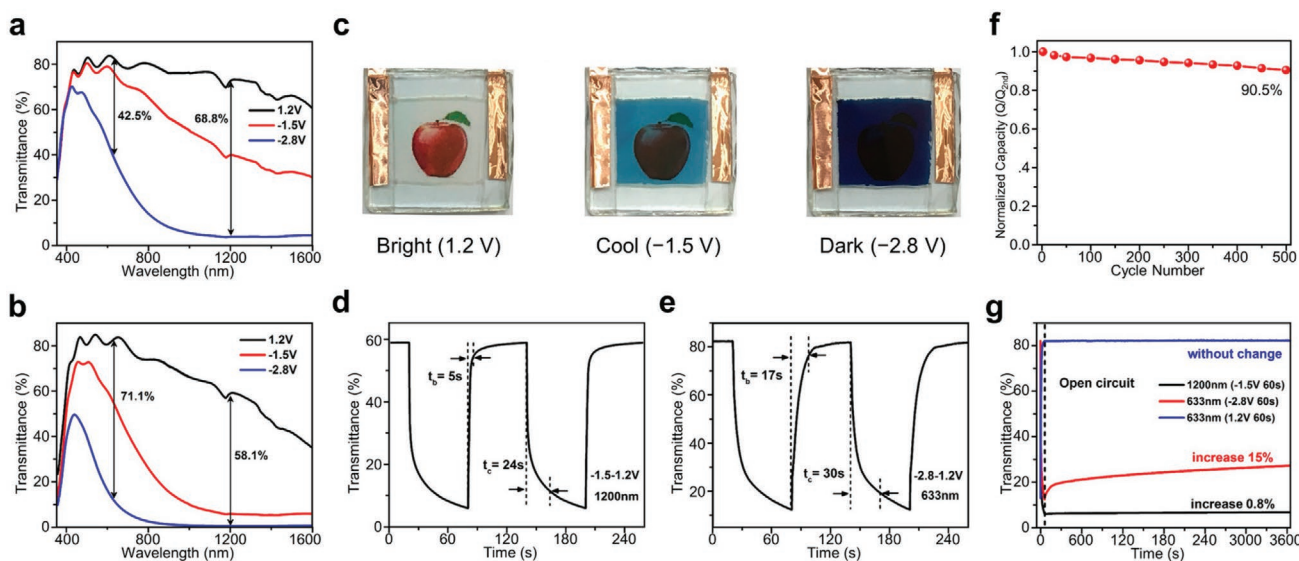


**Figure 7.** Optical and capacity profiles of  $WO_3$ -based films. a) Optical transmittance spectra of the  $WO_3$  (a) and  $WO_3$ -ITO NCs (b) films. c) Digital photos of different modes. d) Real-time transmittance spectra of the device at 1200 (d) and 633 nm (e) in the indicated voltage window. f) The normalized capacity of the device is over 500 voltammetric cycles at  $20 \text{ mV s}^{-1}$ . g) Transmittance changes at 1200 and 633 nm under the open-circuit condition after the device was biased at  $-1.5$ ,  $-2.8$ , and  $1.2 \text{ V}$  for 60 s. All the voltages used in this caption are versus  $Ag^+/Ag$ . Reproduced with permission.<sup>[26]</sup> Copyright 2019, American Chemical Society.

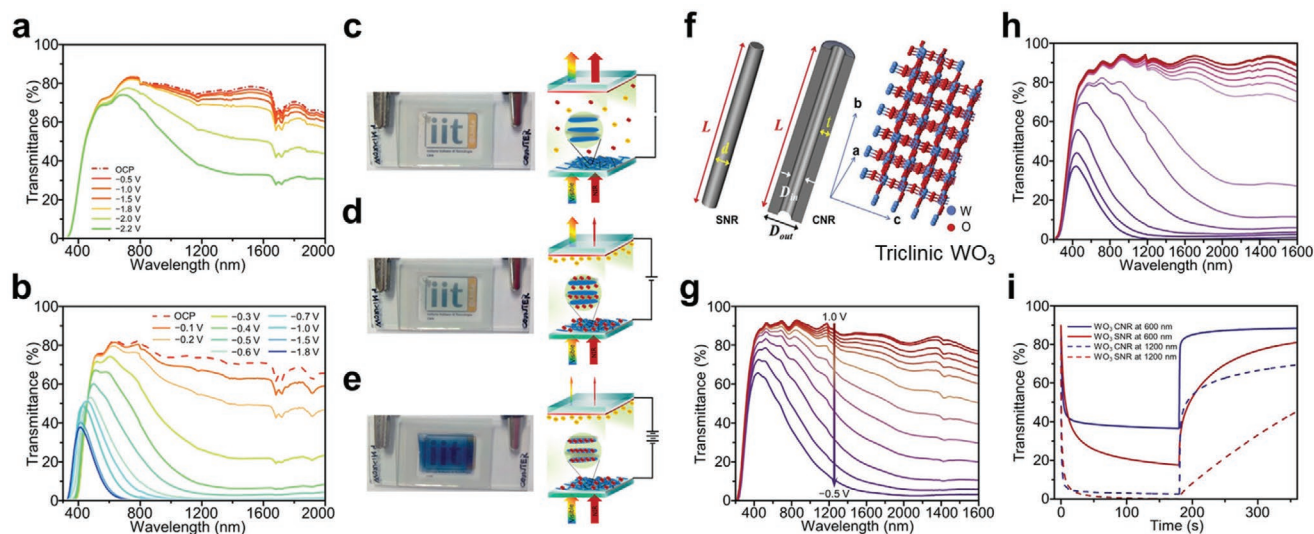


**Figure 8.** Structure profile, EC behavior, and proposed mechanism of  $\text{WO}_3$ -based EC films. The transmittance spectra of  $\text{WO}_3$  NR film filled with a) 1 M  $\text{LiClO}_4$  and b) 0.7 M  $\text{LiClO}_4$  + 0.3 M  $\text{LiI}$  at indicated voltages. c–e) Sketch of a  $\text{WO}_3$ -NR-based EC device in three different operative conditions (at OCP,  $-1.4$ , and  $-1.8$  V, versus  $\text{AgCl}/\text{Ag}$ ). Reproduced with permission.<sup>[25]</sup> Copyright 2016, Royal Society of Chemistry. f) Schematic structures of  $\text{WO}_3$  SNR and CNR with triclinic phase. Optical transmittance spectra of g)  $\text{WO}_3$  CNR-film and h)  $\text{WO}_3$  SNR-film of  $1.2 \mu\text{m}$  thickness, the voltages from top to bottom: 1.0, 0.8, 0.6, 0.4, 0.3, 0.2, 0.1, 0,  $-0.1$ ,  $-0.2$ ,  $-0.3$ ,  $-0.4$ , and  $-0.5$  V (versus  $\text{AgCl}/\text{Ag}$ ). i) In situ transmittance profiles of two films at 600 and 1200 nm under a successive voltage of 1.0 and  $-0.5$  V (versus  $\text{AgCl}/\text{Ag}$ ) for 180 s, respectively. Reproduced with permission.<sup>[29]</sup> Copyright 2017, Elsevier Ltd.

(versus  $\text{Ag}^+/\text{Ag}$ ). After a 6-layer ITO NC film anode was paired with the  $\text{WO}_{3-x}$  cathode, there was a comparable NIR contrast along with an unexpected but much-improved VIS contrast (71.1%) (Figure 7b) due to the more effective charge balancing action of a 6-layer ITO NC film, resulting in greater optical modulation. The optimized dual-band EC device assembled from a  $\text{WO}_{3-x}$  cathode and an ITO NCs anode delivered three distinct operating modes (Figure 7c)-bright, cool, and dark-with high optical modulation, fast color switching (Figure 7d,e), good cycle stability (Figure 7f), and bistability (Figure 7g).

### 2.1.2. Single-Component EC Materials

Currently, most of the reported dual-band EC materials are complex composites which are fabricated via the delicate integration of NIR-selective and VIS-active components.<sup>[83]</sup> Realization of the selective modulation of VIS and NIR light on single component active materials would thus greatly simplify the manufacturing process and the structure of the EC devices.  $\text{WO}_{3-x}$  NCs have been reported to deliver the selective modulation of NIR light<sup>[84]</sup> due to voltage-tunable LSPR absorption in NIR regions induced by oxygen vacancies within the lattice and variable concentration of free electrons.<sup>[23]</sup> In combination with the intrinsic VIS-regulating capacity of traditional  $\text{WO}_3$  materials induced by the diffusion-controlled ionic insertion/deinsertion at high potentials, similar to that of  $\text{Nd-TiO}_2$ ,<sup>[85]</sup> it is feasible to fabricate a  $\text{WO}_3$ -based single-component dual-band EC device.

As early as 2015, Manca et al. proposed a single-component dual-band EC device based on near-stoichiometric  $\text{WO}_3$  nanorods (NRs) with high aspect-ratios, synthesized from thermal annealing of  $\text{W}_{18}\text{O}_{49}$  NRs in air at  $400^\circ\text{C}$ , accompanied by the structure transformation from monoclinic to triclinic

phase. The  $\text{WO}_3$  NRs-based EC cells exhibited a modest NIR modulation with an overall contrast of 28%, but no detectable VIS modulation capacity using 1 M  $\text{LiClO}_4$  as the electrolyte (Figure 8a). Interestingly, using a mixture of 0.7 M  $\text{LiClO}_4$  and 0.3 M  $\text{LiI}$  as the electrolyte, resulted in significantly improved performance of enhanced modulation contrast in NIR regions from 46.8% to 99.8%, extended modulation range driven by a narrower potential range (Figure 8b), and dramatically increased optical switching speed. Such enhanced dual-band EC performance was ascribed to the following Pt-catalyzed redox reaction:  $3\text{I}^- \leftrightarrow \text{I}_3^- + 2\text{e}^-$ , as large faradaic currents during the redox reactions can trigger electron injection into the  $\text{WO}_3$  lattice and capacitive surface charging.<sup>[86–87]</sup> Figure 8c–e shows the principle of  $\text{WO}_3$  NR-based EC devices in three different states. At open circuit potential (OCP),  $\text{WO}_3$  is almost transparent, allowing for most VIS and NIR components to pass through the device, leading to a bright state (Figure 8c). At moderate potentials, massive electrons generated from the redox reaction are rapidly injected into  $\text{WO}_3$ , leading to a higher accumulation of  $\text{Li}^+$  ions around the surface of the  $\text{WO}_3$  NRs instead of deeply intercalating into the lattice. The resulting surface capacitance causes a dramatic increase in NIR absorption but a negligible change in VIS contrast, causing a cool state (Figure 8d). At higher potentials,  $\text{Li}^+$  intercalation into  $\text{WO}_3$  lattice induces an intense absorption in the VIS region in addition to the significant NIR absorption, resulting in a dark state (Figure 8e). This study demonstrated the possibility that the selective and independent modulation over NIR and VIS regions could take place within a single component EC device.<sup>[25]</sup> Studies aim at substituting  $\text{I}^-/\text{I}_3^-$  couples are also in progress to solve the drawbacks of iodine-based redox electrolyte.<sup>[88]</sup>

The EC response of  $\text{WO}_3$ -based films is highly dependent on the structure and geometry of the  $\text{WO}_3$  NCs because they directly influence the surface-to-volume ratio, ion-diffusion distances,



**Table 1.** Comparison of the important parameters of recent dual-band EC films/devices.

EC materials	Size [nm, component]	Electrolytes	$E$ [V, vs $\text{Li}^+/\text{Li}$ ]	$t_c/t_b$ [s] at $\lambda$ [nm]	Contrast at $\lambda$ [nm]	Cycles (optical loss)	Ref.
ITO NC// $\text{WO}_{3-x}$ NW device	$8.6 \pm 0.9$ (ITO)	$\text{Al}(\text{ClO}_4)_3/\text{PC}$	$-2.8 \approx 1.2^{\text{a}}$	30/17 (633)	71.1% (633) 58.1% (1200)	500 (9.5%) <sup>d</sup>	[26]
$\text{W}_{18}\text{O}_{49}$ NW- $\text{P}_8\text{W}_{48}$ film	10–20 nm $\times$ several $\mu\text{m}$ ( $\text{W}_{18}\text{O}_{49}$ )	$\text{LiClO}_4$	$-1.0 \approx 0.4^{\text{b}}$	52/ (1060) 26/86 (500)	60% (1060) <sup>j</sup> 40% (500) <sup>j</sup>	500 (3.2% at 1060 nm, 2.4% at 500 nm)	[23]
Nb- $\text{TiO}_2$ NC film	11	Li-TFSI/TG	$1.5 \approx 4$	–	–	–	[85]
ITO NC-in- $\text{NbO}_x$ film	$4.8 \pm 0.8$ (ITO)	$\text{LiClO}_4/\text{PC}$	$1.5 \approx 4$	–	–	2000 (4%) <sup>d</sup>	[65]
$\text{WO}_{3-x}$ NC- $\text{NbO}_x$ film	$4.3 \pm 1.3$ ( $\text{WO}_{3-x}$ )	Li-TFSI	$1.5 \approx 4$	–	71% (VIS) 84% (NIR)	2000 (5.7%) <sup>d</sup>	[64]
$\text{WO}_{3-x}$ NR film	$60 \times 3$	$\text{LiClO}_4$	$-2.2 \approx 0^{\text{b}}$	220/260 (1500)	44.3% (1500)	–	[25]
m- $\text{WO}_{3-x}$ NW film	$30 \times 2.5$	$\text{LiClO}_4 + \text{LiI}$	$-1.8 \approx 0^{\text{b}}$	8/105 (1500)	80.1% (800)	500 (5% at 1500 nm)	[89]
		0.5 M Li-TFSI/TG	$2 \approx 4$	21/85 (633) 22/75 (1200)	91.7% (633) 92.7% (800) 94.6% (1200) 87.3% (1600)	1000 (8.3% at 633 nm) 1000 (20%) <sup>d</sup>	
$\text{WO}_3$ CNR film	$(8.5-2.5)^{\text{j}}$ $\times$ 80	$\text{LiClO}_4/\text{PC}$	$-0.5 \approx 1^{\text{b}}$	16/13 (633)	93.2% (633)	2000 (5.5%) <sup>d</sup>	[27]
				8/5 (1200)	91.7% (800) 88.5% (1200) 86.8% (1600)		
$\text{WO}_3$ SNR film	$3 \times 80$	$\text{LiClO}_4/\text{PC}$	$-0.5 \approx 1^{\text{b}}$	21/85 (633)	93.1% (800) <sup>e</sup>	500 (10%) <sup>d,i</sup>	[29]
				3/360 (1200)	88.6% (1200) <sup>e</sup> 81.3% (1600) <sup>e</sup>		
$\text{WO}_3$ SNR film	$3 \times 80$	$\text{LiClO}_4/\text{PC}$	$-0.5 \approx 1^{\text{b}}$	98/>1200 (600)	80% (600)	500 (17%) <sup>d,i</sup>	[29]
				8/>3600 (1200)	89% (1200) 93% (700-1600)		
$\text{W}_{18}\text{O}_{49}/\text{PB}$ film	–	$\text{LiClO}_4/\text{PC}$	$-1.5 \approx 1^{\text{b}}$	2.2/4.2 (633)	71.2% (633) 64.8% (1600)	100 (30% at 633 nm, 42% at 1600 nm)	[46]
Nb- $\text{TiO}_2$ NC film	$\approx 10$	$\text{LiClO}_4/\text{PC}$	$-4 \approx 0^{\text{b}}$	105/<8 <sup>f</sup> (500) 10/<8 <sup>f</sup> (2000)	64% (800-2000) 67% (2000)	–	[92]
Ta- $\text{TiO}_2$ NC film	$11.6 \pm 1.4$	Li-TFSI/TG	$1.5 \approx 4$	66.8/6.9 (550) 18.4/1.1 (1600)	86.3% (550) 81.4% (1600)	2000 (14.8%) <sup>d</sup>	[101]
Ta- $\text{TiO}_2$ NC film	$11.2 \pm 1.1$	$\text{LiClO}_4/\text{PC}$	$1.5 \approx 3.5$	52.6/9.5 (550)	89.1 (550)	2000 (4.1%) <sup>d</sup>	[28]
				11.4/3.6 (1600)	81.4 (1600)		
Ta- $\text{TiO}_2$ NC device	–	–	$-3.5 \approx 1$	–	72.7 (550) 62.2 (1600)	–	–
$\text{TiO}_{2-x}$ NC film	$7.82 \pm 1.5$	$\text{LiClO}_4/\text{PC}$	$1.5 \approx 3.5$	35.1/9.6 (633)	95.5 (633)	2000 (4.4%) <sup>d,k</sup>	[24]
				15.5/3.4 (1600)	98.8 (800) 90.5 (1200) 77.5 (1600)		
$\text{TiO}_{2-x}$ NC device	–	–	$-3.2 \approx 1$	–	74.5 (633) 73.2 (800) 69.2 (1200) 75 (1600)	500 (10.2%) <sup>d</sup>	–
$\text{WO}_3$ NC// $\text{VTiO}_2$ NC film	5 ( $\text{VTiO}_2$ )	$\text{LiClO}_4 + \text{LiI}$ in DMSO	$-2.2 \approx 2.7^{\text{b}}$	–	–	–	[93]
$\text{WO}_3$ // $\text{VO}_2$ NC film	–	$\text{LiTaO}_3$	$-4 \approx 4$	15/5 (580)	–	–	[42]
ITO/PTs composites film	$\approx 5$ (ITO)	$\text{LiClO}_4/\text{PC}$	$-1.25 \sim 1.25^{\text{c}}$	68/19 (700) <sup>g</sup> 33/71 (1350) <sup>g</sup>	22% (700) <sup>h</sup> 39% (1250) <sup>j</sup>	200 (18% at 700 nm, 15% at 1350 nm)	[121]

**Table 1.** Continued.

EC materials	Size [nm, component]	Electrolytes	$E$ [V, vs $\text{Li}^+/\text{Li}$ ]	$t_c/t_b$ [s] at $\lambda$ [nm]	Contrast at $\lambda$ [nm]	Cycles (optical loss)	Ref.
PANI-ITO NC composites film	10 (ITO NCs)	$\text{LiClO}_4/\text{PC}$	$-1.0 \approx 1.2^{\text{b}}$	19/6 (500) 4/14 (600) 7/28 (1000)	$\approx 80\%$ (1600)	–	[127]
$\text{NbO}_x$ -ITO film	$\approx 5$	Li-TFSI/TG	$1.5 \approx 4.0$	–	–	1000 (5%) <sup>d)</sup>	[107]
TPPT film	–	Li-TFSI	$-1.0 \approx 0^{\text{c}}$	13.4/21.5 (887) 19.1/13.8 (600)	66.63% (887) 50.71% (600)	–	[43]
TPBT film	–	Li-TFSI	$-1.0 \approx 0^{\text{c}}$	27.4/24.3 (900) 22.0/20.8 (600)	59.79% (900) 66.90% (600)	–	

<sup>a)</sup>versus  $\text{Ag}^+/\text{Ag}$ ; <sup>b)</sup>versus  $\text{AgCl}/\text{Ag}$ ; <sup>c)</sup>versus  $\text{Fc}^+/\text{Fc}$ ; <sup>d)</sup>Charge capacity loss; <sup>e)</sup>After 2000 cycles; <sup>f)</sup>Measured at +1 V, estimated from the Figure 11c; <sup>g)</sup>Half switching time; <sup>h)</sup>Between “bright” and “dark” modes; <sup>i)</sup>Between “bright” and “cool” modes; <sup>j)</sup>Estimated based on the original publications; <sup>k)</sup>Measured in TBA-TFSI/PC electrolyte; <sup>l)</sup>Outer diameter–inner concavity width (see Figure 8f).  $t_c$ : the duration of coloring process;  $t_b$ : the duration of the bleaching process; PTP: polythiophene; Li-TFSI/TG: bis(trifluoromethane)sulfonimide lithium in tetraglyme; CNR: solid nanorod; CNR: carved nanorod; TPPT: 2,4,6-tri(pyridyl-4-propyl)-1,3,5-triazine bromide; TPBT: 2,4,6-tri(pyridyl-4-benzyl)-1,3,5-triazine bromide.

and charge-storage mechanism.<sup>[29]</sup> Two sets of triclinic  $\text{WO}_3$  NRs with solid and carved structures (SNRs and CNRs, Figure 8f) featuring identical crystal structure and lattice orientation were synthesized to investigate the influence of architecture on the EC performance. As shown in Figure 8g,h, compared to the  $\text{WO}_3$  CNR-film, the  $\text{WO}_3$  SNR-film exhibited improved modulation contrast and a wider optical-responsive range at identical potentials (Table 1). Such a difference in optical responses was ascribed to the higher overall charge density on the  $\text{WO}_3$  SNR-film, which could accommodate a larger amount of charge. On the other hand, the switching rates of the  $\text{WO}_3$  CNR-film during the coloring and bleaching processes at 600 and 1200 nm were much faster than those of  $\text{WO}_3$  SNR ones (Figure 8i) due to the dominant pseudocapacitive behavior of CNR-film, which was highly related to the peculiar nanostructure.

To further improve the EC performance of the  $\text{WO}_3$ -based device, Lee et al. reported a single-component material, monoclinic  $\text{WO}_{3-x}$  ( $m\text{-WO}_{3-x}$ ) NW-based dual-band EC device and

systematically investigated its EC mechanism. As shown in Figure 9a, the  $m\text{-WO}_{3-x}$  film was highly transparent for both NIR and VIS at 4 V (versus  $\text{Li}^+/\text{Li}$ , bright mode). When the voltage was decreased from 4 to 2.8 V, the NIR absorption was enhanced by the LSPR effect from capacitive charging induced by  $\text{Li}^+$  adsorption. In the range from 2.8 to 2.6 V, the film blocked most NIR while keeping a high VIS transmittance of 64.6%, which was attributed to the  $\text{Li}^+$  intercalation into  $m\text{-WO}_{3-x}$  lattice, evidenced by the phase transition from  $m\text{-WO}_{3-x}$  to tetragonal  $\text{LiWO}_{3-x}$  ( $t\text{-LiWO}_{3-x}$ ) (Figure 9c), resulting in a cool mode (Figure 9d) with 95.8% of NIR blocked (Figure 9a). At 2 V, 88.5% of VIS and almost all the NIR can be blocked (dark mode) (Figure 9a,d). The VIS modulation was attributed to the bandgap transitions between  $t\text{-LiWO}_{3-x}$  and cubic  $\text{LiWO}_{3-x}$  ( $c\text{-LiWO}_{3-x}$ ) (Figure 9c). Therefore, the  $m\text{-WO}_{3-x}$  NW films can work in three distinct modes with an overall 20% of capacity loss after 1000 cycles. Nevertheless, the long switching time (>20 s for coloration and >75 s for bleaching, Figure 9b) and inferior cycle stability still hinder the development of the

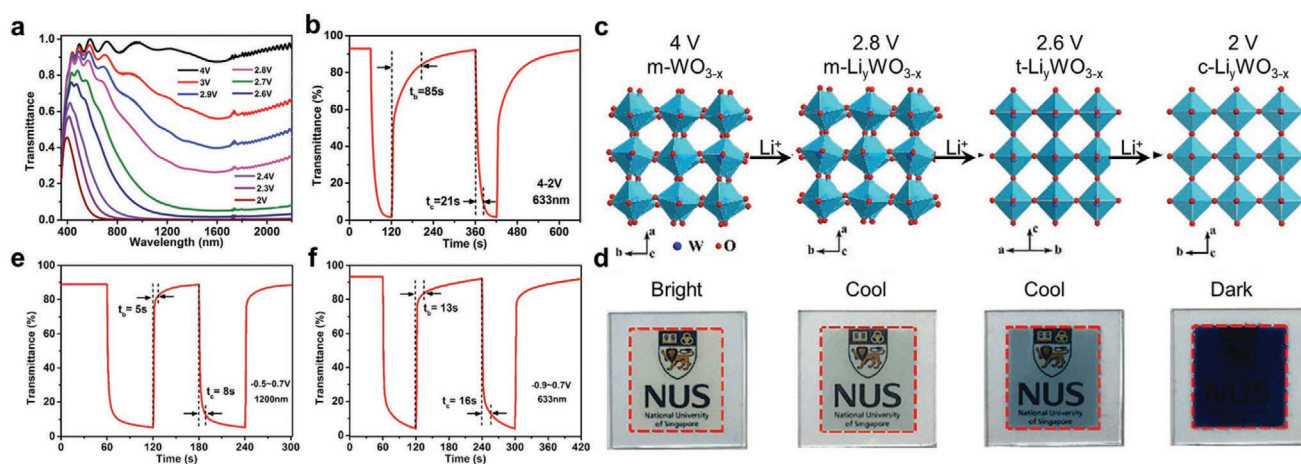


**Figure 9.** EC performance and structural evolution of  $\text{WO}_3$ -based EC films. a) Optical transmittance spectra of the  $m\text{-WO}_{3-x}$  NW film. b) Optical transmittance of  $m\text{-WO}_{3-x}$  NW films in the potential of between 4 and 2 V (versus  $\text{Li}^+/\text{Li}$ ). Crystal structures evolution c) and digital photos d) of  $m\text{-WO}_{3-x}$  NW films at 4, 2.8, 2.6, and 2 V, respectively. The  $\text{Li}^+$ -containing electrolyte was used in Figure 9a–d. Reproduced with permission.<sup>[89]</sup> Copyright 2018, Royal Society of Chemistry. Real-time transmittance spectra of  $m\text{-WO}_{3-x}$  NW films e) at 1200 nm between  $-0.5$  and  $0.7$  V (versus  $\text{Ag}^+/\text{Ag}$ ) and f) at 633 nm between  $-0.9$  and  $0.7$  V, using an  $\text{Al}^{3+}$ -containing electrolyte (Figure 9e–f). Reproduced with permission.<sup>[27]</sup> Copyright 2018, Royal Society of Chemistry.

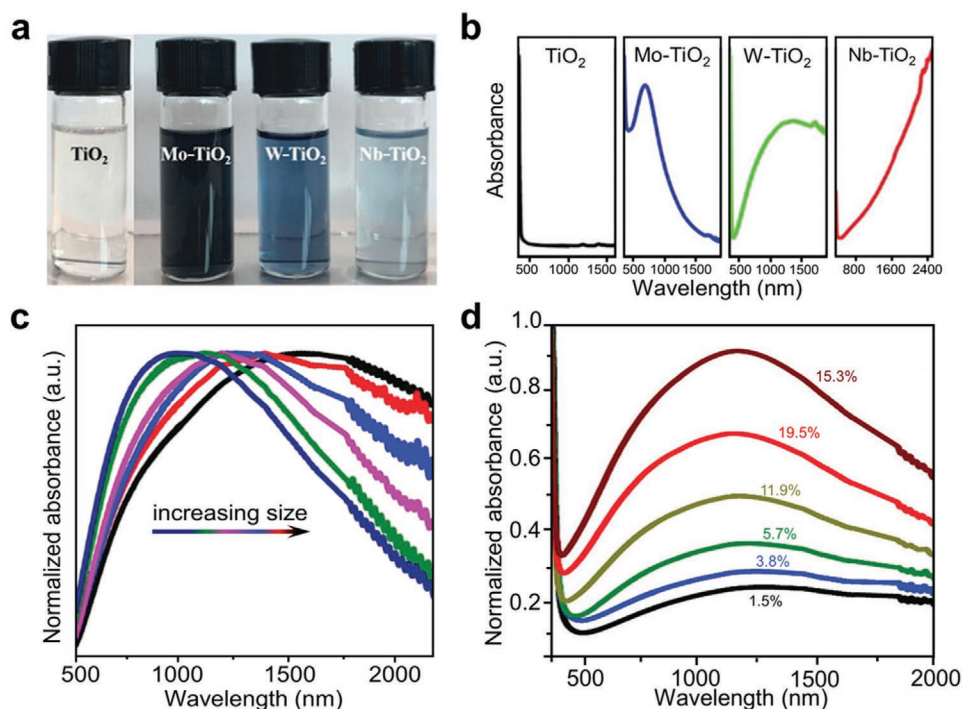


**Figure 10.** Photographs and absorption spectra of the metal-doped  $\text{TiO}_2$ . a) Digital photos and b) UV-vis-IR absorption spectra of pristine  $\text{TiO}_2$ ,  $\text{Mo-TiO}_2$ ,  $\text{W-TiO}_2$ , and  $\text{Nb-TiO}_2$  NCs. c) Normalized absorption spectra of  $\text{W-TiO}_2$  NCs synthesized of different sizes. d) Intensity (at 350 nm)-based normalized absorption spectra of  $\text{W-TiO}_2$  NCs with various W dopant concentrations. Reproduced with permission.<sup>[98]</sup> Copyright 2018, American Chemical Society.

dual-band EC device.<sup>[89]</sup> However, the same group soon reported a similar dual-band EC system with much-improved switching speed and stability by using earth-abundant trivalent ions  $\text{Al}^{3+}$  as insertion ions instead of  $\text{Li}^+$ .<sup>[27]</sup> In spite of the low diffusion coefficient of  $\text{Al}^{3+}$  ( $7.6 \times 10^{-11} \text{ cm}^2 \text{ s}^{-1}$ ) in  $\text{m-WO}_{3-x}$  NWs compared with that of  $\text{Li}^+$  ( $6 \times 10^{-10} \text{ cm}^2 \text{ s}^{-1}$ ),  $\text{Al}^{3+}$  has a smaller ionic radius (0.53 Å) than that of  $\text{Li}^+$  (0.76 Å), which is highly advantageous for  $\text{Al}^{3+}$  diffusion into the lattice of host materials. Furthermore, trivalent  $\text{Al}^{3+}$  ions are able to transfer up to three electrons, resulting in one-third of the amount  $\text{Li}^+$  required to be intercalated to balance the charge from the same amount of the electrons. This substantially reduced amount of intercalated  $\text{Al}^{3+}$  plays a significant role in improving the switching speed (Figure 9e,f), coloration efficiency, and, especially, the cycle stability (94.5% of capacity remained after 2000 cycles) of  $\text{m-WO}_{3-x}$  NWs.<sup>[27]</sup>

## 2.2. $\text{TiO}_2$ -Based Dual-Band EC Materials

$\text{TiO}_2$  NCs are a well-known  $\text{Li}^+$  host material<sup>[90–92]</sup> that have been reported as another promising candidate as active EC material<sup>[93]</sup> because of their large ion-bearing capacity, high abundance, and excellent chemical and thermal stability.<sup>[94]</sup> Pristine anatase  $\text{TiO}_2$  (a- $\text{TiO}_2$ ) NCs show no absorption in VIS and NIR range due to their large bandgap. But upon  $\text{Li}^+$  intercalation, a- $\text{TiO}_2$  exhibits VIS extinction due to the localization of injected electrons on Ti cations<sup>[94]</sup> by creating a polaronic lattice distortion.<sup>[95–96]</sup> Encouragingly, similar to  $\text{WO}_3$ , the LSPR frequency of  $\text{TiO}_2$  can also be broadly tuned by alivalent doping.<sup>[75]</sup> In 2013,

Milliron et al. reported that Niobium-doped  $\text{TiO}_2$  ( $\text{Nb-TiO}_2$ ) synthesized through a hot injection method improved carrier density in the conduction band due to the substitution of  $\text{Nb}^{5+}$  on  $\text{Ti}^{4+}$  sites, resulting in a broad LSPR absorption.<sup>[97]</sup> Recently, Cao et al. reported that the LSPR absorption peaks of Mo-, W-, and Nb-doped  $\text{TiO}_2$  ( $\text{Mo-TiO}_2$ ,  $\text{W-TiO}_2$ , and  $\text{Nb-TiO}_2$ ) appear at 650 nm (VIS), 1190 nm (NIR), and  $\approx 3300$  nm (mid-IR), respectively (Figure 10a,b), in accordance with their free electron concentrations of approximately  $1.61 \times 10^{22}$ ,  $4.81 \times 10^{21}$ , and  $6.26 \times 10^{20} \text{ cm}^{-3}$  for  $\text{Mo-TiO}_2$ ,  $\text{W-TiO}_2$ , and  $\text{Nb-TiO}_2$ , respectively.  $\text{W-TiO}_2$  exhibited the most tunable LSPR absorption peaks, shifting from 1700 to 980 nm by reducing the particle size, which was ascribed to the increased energy of intraband transitions (Figure 10c). The LSPR absorption intensities are also associated with the doping concentrations of W (Figure 10d), which changes the number of electrons near the Fermi level.<sup>[98]</sup> Therefore, tunable extinction of  $\text{TiO}_2$  NCs can be easily achieved by changing both the dopant types and concentrations as well as the particle size of  $\text{TiO}_2$ , leading to their increased exploration as active materials or key components in dual-band EC devices.

### 2.2.1. Single-Component EC Materials

Similar to the earlier discussed  $\text{WO}_3$ , metal-doped  $\text{TiO}_2$  has been regarded as another promising active material for dual-band EC devices due to the combined effects of capacitive LSPR caused by synthetic doping/electrochemical reduction and ion-intercalation induced VIS absorption.<sup>[99–100]</sup> VB and

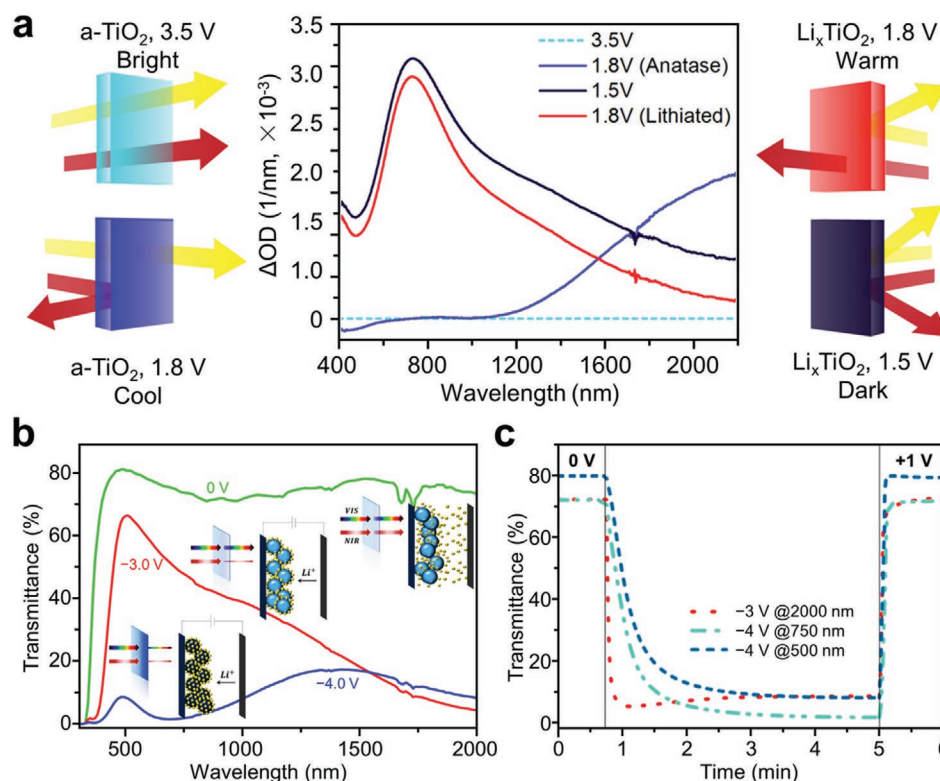


**Figure 11.** Optical performance and working principle of the TiO<sub>2</sub>-based EC film and device. a) In situ absorption spectra normalized by film thickness and the schematic diagram of 5% Nb-doped TiO<sub>2</sub> NC films of four distinct EC modes under indicated voltages. Yellow and red arrows are for visible and NIR light, respectively. Reproduced with permission.<sup>[85]</sup> Copyright 2015, American Chemical Society. b) Transmittance spectra and mechanism of Nb-TiO<sub>2</sub>-based EC device at indicated potentials. c) Time variation of the optical transmittance at 500, 750, and 2000 nm. Reproduced with permission.<sup>[92]</sup> Copyright 2017, American Chemical Society.

VIB metals, such as Nb and Ta, have been used as dopants to regulate the LSPR of TiO<sub>2</sub> to develop TiO<sub>2</sub>-based dual-band EC devices.<sup>[28,92,101]</sup> For the first time in 2015, Dahlman et al. proposed a model of Nb-doped TiO<sub>2</sub> (Nb-TiO<sub>2</sub>)-based dual-band EC film that supported LSPR-modulation in NIR regions through capacitive charging and structural phase transition-caused VIS modulation between tetragonal and orthorhombic lattice phases upon intercalation and extraction of Li<sup>+</sup>. As shown in **Figure 11a**, the Nb-TiO<sub>2</sub> NC film could afford four distinct EC modes including bright (3.5 V, versus Li<sup>+</sup>/Li), cool (1.8 V), dark (1.5 V), and warm (1.8 V).<sup>[85]</sup> However, in this work, the cool and warm modes of Nb-TiO<sub>2</sub> associated with the distinct structural phases under identical potential can only be accessed via reduction from the bright mode and oxidation from the dark mode, respectively (Figure 11a), which makes it highly inconvenient to switch between those modes. Later on, an Nb-TiO<sub>2</sub>-based dual-band EC device filled with a redox electrolyte with a direct optical modulation was fabricated by Barawi et al.<sup>[92]</sup> Investigation of the EC features of Nb-TiO<sub>2</sub> NCs with various Nb doping levels found that optical modulation of the TiO<sub>2</sub> film in the NIR region increases with increasing Nb doping concentration from 0 to 10% under a potential range between 0 and -1.6 V (versus AgCl/Ag). However, 15% Nb doping leads to an inferior optical contrast in the NIR region, indicating that Nb doping from 10% to 15% did not increase the overall density of free carriers, which could be ascribed to the Burstein-Moss effect.<sup>[102]</sup>

The EC device fabricated using 10% Nb-doped TiO<sub>2</sub> had large optical modulation in the NIR region in the potential range from 0 to -3 V (versus AgCl/Ag), which was ascribed to the formation of oxidized iodide species. In addition, in this potential range, Li<sup>+</sup> accumulated around the surface of TiO<sub>2</sub> NCs to balance the injected electrons instead of deeply intercalating into the TiO<sub>2</sub> lattice, which generates LSPR absorption in the NIR region. At a potential range from -3 to -4 V, the intense polaron absorption in the VIS region was driven by massive Li<sup>+</sup> insertion (Figure 11b). Moreover, the as-fabricated EC device showed relatively high switching speeds and coloring times of 10 s at 2000 nm and 105 s at 500 nm (Figure 11c).<sup>[92]</sup> It has been reported that the doping efficiency of metal in the TiO<sub>2</sub> host has a great influence on its LSPR performance, especially when the ionic radius between doped ions and Ti<sup>4+</sup> is very different.<sup>[98]</sup> Ta-doped TiO<sub>2</sub> has been theoretically predicted to have a high density of free electrons, which could greatly improve the LSPR property. However, the ionic diameter mismatch between Ta<sup>5+</sup> (1.28 Å) and Ti<sup>4+</sup> (1.20 Å) is significant, which makes synthesis of Ta-doped TiO<sub>2</sub> difficult.<sup>[100]</sup> To improve the doping efficiency and uniformity of Ta into a TiO<sub>2</sub> host, Cao et al. developed an F-assisted synthesis of Ta-doped TiO<sub>2</sub> (Ta-TiO<sub>2</sub>) NCs for dual-band EC modulation. In the presence of in situ generated HF derived from NH<sub>4</sub>F, TiO<sub>2</sub> NCs will preferentially expose anatase facets, leading to a strong absorption interaction with Ta. This results in improved doping efficiency and distribution

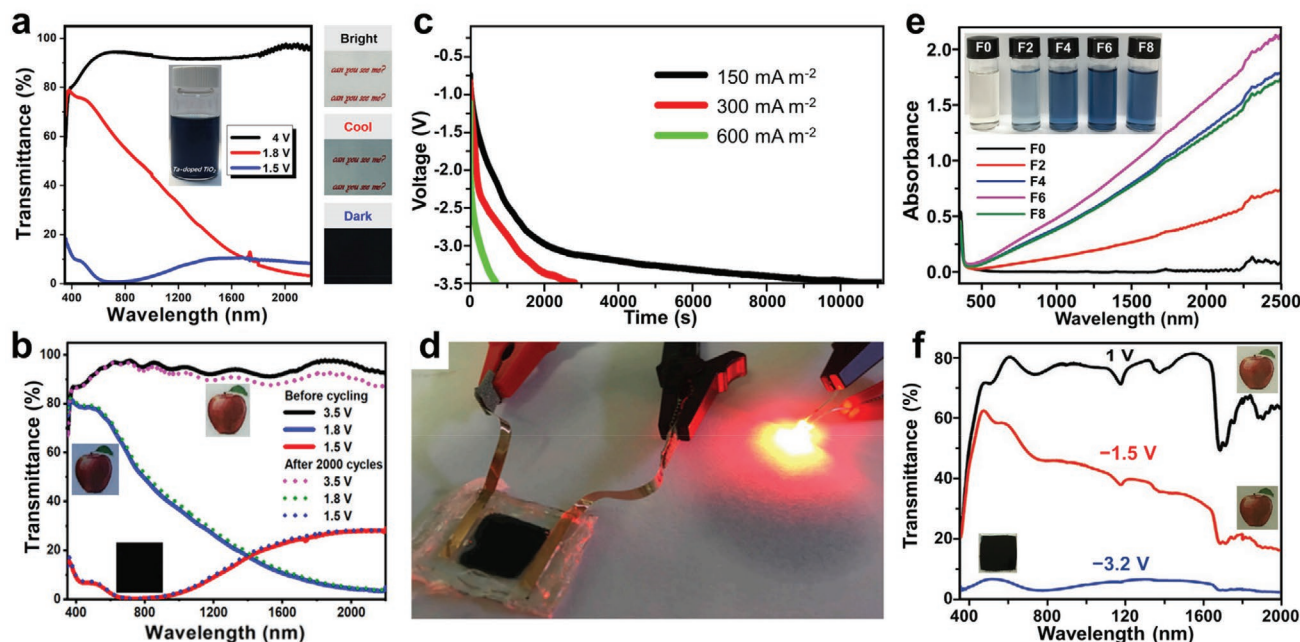


**Figure 12.** EC performance and energy storage profiles of  $\text{TiO}_2$ -based EC film and device. a) Transmittance spectra and corresponding photographs of Ta- $\text{TiO}_2$  film on different modes. Inset: the picture of Ta- $\text{TiO}_2$  solution. Reproduced with permission.<sup>[101]</sup> Copyright 2018, American Chemical Society. b) Transmittance spectra of a Ta- $\text{TiO}_2$  film before and after 2000 cycles. Insets: the pictures of EC film in different modes. c) Galvanostatic charging curves of the EC device at different current densities. d) A photograph of the device powering a red LED. Reproduced with permission.<sup>[28]</sup> Copyright 2019, Elsevier Ltd. e) Absorption spectra and photograph (inset) of colloidal  $\text{TiO}_{2-x}$  NCs solutions synthesized in the presence of different concentrations of  $\text{F}^-$  (F0, F2, F4, F6, and F8: the ratios of F to Ti in precursor mixtures are 0, 0.2, 0.4, 0.6, and 0.8, respectively). f) Transmittance spectra and corresponding photographs (insets) of the all-solid-state dual-band EC device fabricated from  $\text{TiO}_{2-x}$  NCs on different modes. Reproduced with permission.<sup>[24]</sup> Copyright 2020, Wiley-VCH.

uniformity of Ta in the  $\text{TiO}_2$  host, which can be confirmed by the much lower content of Ta in Ta- $\text{TiO}_2$  NCs prepared without  $\text{NH}_4\text{F}$  and the consistent Ta contents on the surface and in the bulk of Ta- $\text{TiO}_2$ , respectively. Consequently, the substitution of  $\text{Ti}^{4+}$  by  $\text{Ta}^{5+}$  contributed to increased concentrations of free electrons that can activate LSPR absorption of  $\text{TiO}_2$  in the NIR region. The as-fabricated Ta- $\text{TiO}_2$  films exhibited large optical contrasts for the VIS (86.3% at 550 nm) and NIR light (81.4% at 1600 nm) (Figure 12a), with coloring and bleaching times of 66.8 and 6.9 s at 550 nm and 18.1 and 1.1 s at 1600 nm, respectively, suggesting that F-assisted synthesis of Ta- $\text{TiO}_2$  NCs are a promising dual-band EC material.<sup>[101]</sup>

The integration of dual-band EC features and energy storage functions into a single device is a promising approach to constructing energy-efficient buildings. The same group further developed their Ta- $\text{TiO}_2$  NCs EC material into a dual-band EC device with internal energy storage.<sup>[28]</sup> In addition to the independent control over VIS and NIR regions with high contrast, a fast switching speed, and excellent bistability (Figure 12b), the Ta- $\text{TiO}_2$ -based EC device could afford high charge-storage capacities of 1278, 2373, and 466.5  $\text{mAh m}^{-2}$  at current densities of 600, 300, and 150  $\text{Ma m}^{-2}$  (Figure 12c), respectively, and easily light up an LED (Figure 12d). The Ta- $\text{TiO}_2$  NCs-based EC device showed great potential in the next generation dual-band EC windows with energy storage function. It has also been reported that metal doping can impact the structural stability of the host materials and increase the ion diffusion barrier

in the host lattice due to lattice strain and distortion.<sup>[92,100]</sup> In addition to aliovalent substitutional doping, the introduction of O-vacancy can also improve the EC behavior of  $\text{TiO}_2$  by increasing the density of free carriers<sup>[103]</sup> and ion diffusion kinetics.<sup>[104]</sup> Recently, Lee et al. presented an F-assisted synthesis of O-deficient  $\text{TiO}_{2-x}$  NCs, which were then employed for dual-band EC devices.<sup>[24]</sup> The concentration of F in the precursor mixture had a significant impact on the crystalline structure and content of O-vacancies. As shown in Figure 12e, the NIR absorption intensity of  $\text{TiO}_{2-x}$  increased when the ratio of F/Ti increased from 0 to 0.6. The O-vacancies were further demonstrated to improve the  $\text{Li}^+$  diffusion kinetics in  $\text{TiO}_{2-x}$ , which can increase the switching speed. Consequently, optimized  $\text{TiO}_{2-x}$  NC-based film afforded an excellent dual-band EC performance with high optical modulation (95.5% at 633 nm and 90.5% at 1200 nm), high bistability, and long lifecycle. Impressively, these as-synthesized  $\text{TiO}_{2-x}$  NCs have shown great potential in all-solid-state dual-band EC devices (Figure 12f).<sup>[24]</sup>

### 2.2.2. Multi-Component EC Materials

Metal-doped  $\text{TiO}_2$  and  $\text{TiO}_{2-x}$  with O-vacancies as single component active dual-band EC materials have been extensively reported. However, although most  $\text{TiO}_2$ -based single component EC electrodes/devices are able to switch among bright, and dark modes, they are not capable of effectively modulating the

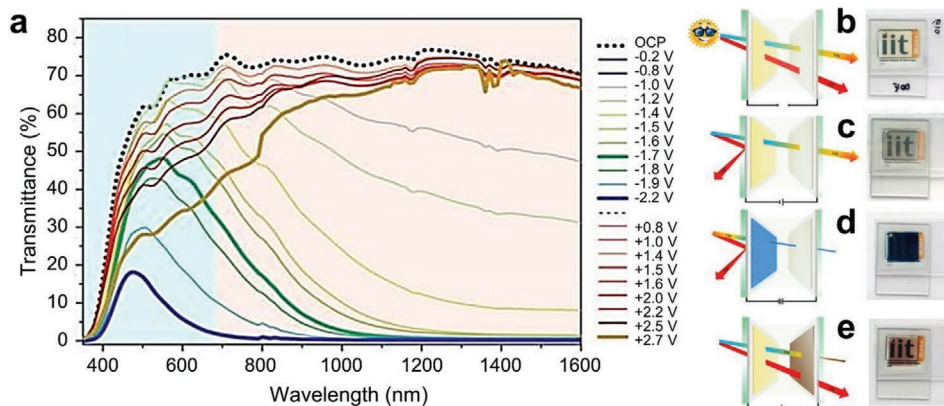


**Figure 13.** EC performance and diagram of the VTiO<sub>2</sub>-WO<sub>3</sub> EC film. a) Transmission spectra of the all-solid-state EC device at indicated potentials (versus AgCl/Ag). b–e) Schematic diagram of the dual-band EC cell combining a WO<sub>3</sub> and a VTiO<sub>2</sub> electrode, and representative pictures of the corresponding device in each of the four different optical states. Reproduced with permission.<sup>[93]</sup> Copyright 2018, Royal Society of Chemistry.

intensity of VIS while keeping a high transmittance of NIR radiation (warm mode), which is favorable to maintaining a comfortable temperature environment while protecting privacy. To help solve this problem, a sandwich EC cell composed of two optically active materials, V-modified TiO<sub>2</sub> (TiO<sub>2</sub> core surrounded by a V-rich TiO<sub>2</sub> shell, VTiO<sub>2</sub>) and WO<sub>3</sub> have been proposed.<sup>[93]</sup> Compared with bare TiO<sub>2</sub>, VTiO<sub>2</sub> film exhibited a broad VIS absorption peak between 400 and 800 nm but no absorption in the NIR region at -0.8 V, which offers an opportunity to modulate VIS light without affecting the transmission of solar heat. On the other hand, under a separate potential range, WO<sub>3</sub> film can selectively block NIR light while maintaining a reasonably high VIS light. Thus, by integrating VTiO<sub>2</sub> and WO<sub>3</sub> into a sandwich EC cell, a dual-band EC cell with four distinct optical modes was fabricated. As shown in Figure 13a, at OCP the cell allows the full penetration of VIS and NIR light (bright mode, Figure 13b). Between 0 and -1.6 V (versus AgCl/Ag), the WO<sub>3</sub> electrode can selectively block NIR radiation (cool mode, Figure 13c). When the potential range was further increased from -1.6 to -2.2 V, the transmittance of VIS light was also greatly blocked, reaching a dark mode (Figure 13d). Importantly, the cell was also able to absorb VIS light while maintaining a high NIR transmittance upon a positive potential (warm mode, Figure 13e). Using this system a dual-band EC cell switchable across four distinct optical modes could be realized.<sup>[93]</sup>

### 2.3. Other Inorganic Metal Oxides

In addition to WO<sub>3</sub>- and TiO<sub>2</sub>-based dual-band EC materials, other metal oxide-based dual-band devices have also been developed. Owing to their higher coloration efficiency, lower growth temperature, and large ion diffusion channels, amorphous metal oxides may be preferred over crystalline ones to fabricate EC films.<sup>[105]</sup> Moreover, enhanced physical and optical properties could be obtained when NCs are formed within an amorphous matrix,<sup>[106]</sup> because it not only combines the functions of two components but also manipulates the crystal structure to change its properties. As early as 2013, Milliron et al. developed precursory dual-band EC films by integrating the VIS- and

the NIR-modulation functions of NbO<sub>x</sub> and ITO, which were composed of ITO NCs embedded in amorphous NbO<sub>x</sub> (ITO-in-NbO<sub>x</sub>, Figure 14a), through a solution deposition method, followed by a thermal annealing treatment at 400 °C. The optical contrast of NbO<sub>x</sub> in the VIS region was enhanced up to five times when the embedded ITO was increased to 43%, which was attributed to the rearranged nanocrystal-linked structure of NbO<sub>x</sub>. For ITO-in-NbO<sub>x</sub>, 96% of charge capacity remained after 2000 cycles, compared to the 80% and 15% observed for pure NbO<sub>x</sub> and ITO, respectively, indicating the superior stability of the ITO-in-NbO<sub>x</sub> composites upon repeated ion insertion and extraction.<sup>[65]</sup> However, the fabrication of amorphous metal oxide-based EC films through solution deposition always requires a high-temperature annealing process, precluding the use of flexible polymeric substrates. To this end, Milliron et al. developed a solution process to fabricate a flexible ITO-in-NbO<sub>x</sub> EC film via an acid-catalyzed condensation of polyniobate clusters at room temperature. The terminal Nb=O bonds in the NbO<sub>x</sub> cluster were protonated to form Nb-OH, which then underwent a condensation reaction to generate Nb-O-Nb bonds between NbO<sub>x</sub> clusters, resulting in a one-dimensional NbO<sub>x</sub> chain (Figure 14b) with greatly improved EC performance. This room-temperature processing method enables the fabrication of ITO-in-NbO<sub>x</sub>-based flexible dual-band EC films (Figure 14c) and full solid-state EC devices (Figure 14d) with only 5% optical loss after 1000 cycles.<sup>[107]</sup>

Similar to EC materials, thermochromic (TC) materials can also control the transmittance of light by changing their colors in response to ambient temperature.<sup>[108–110]</sup> Thus, hybrid systems that integrate EC and TC components are an alternative way to achieve dual-band optical modulation. Kim et al. constructed a VO<sub>2</sub>/Ta<sub>2</sub>O<sub>5</sub>/WO<sub>3</sub>-based dual-band optical device (Figure 15a) through magnetron sputtering. In this system, VO<sub>2</sub> modulated NIR light using the reversible phase change that occurs between monoclinic and rutile phases at a critical temperature of 67 °C, amorphous WO<sub>3</sub> served as the EC component to regulate VIS light in response to external voltage, and Ta<sub>2</sub>O<sub>5</sub> acted as a solid electrolyte. By simultaneously adjusting the voltage and temperature, four different optical states were realized (Figure 15b,c).<sup>[111]</sup> Afterwards, Jia et al. also developed

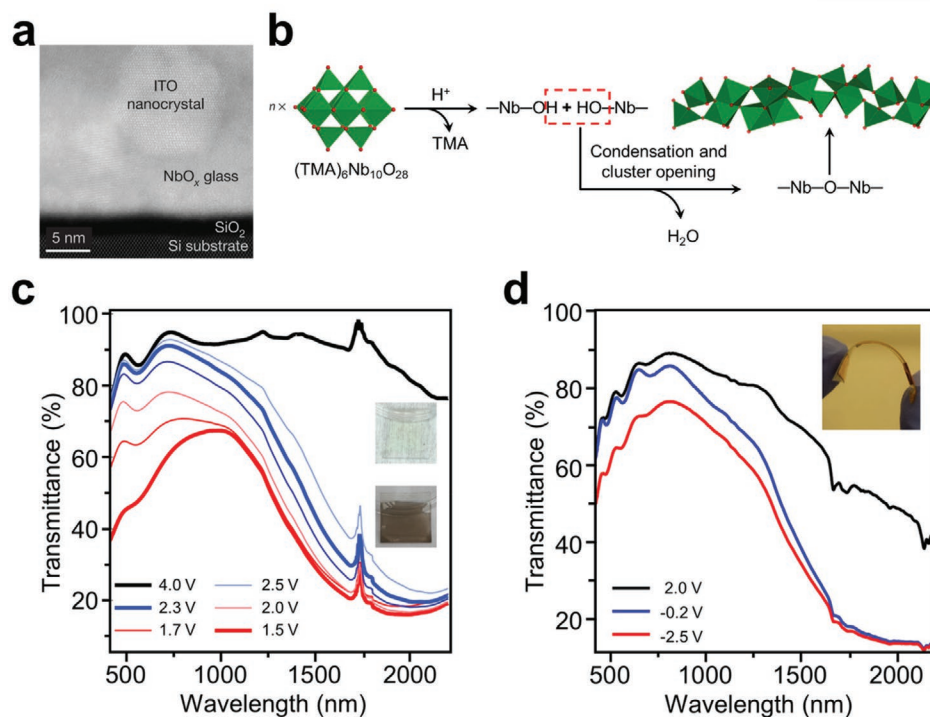


**Figure 14.** Synthesis, structure, and optical behavior of the ITO-in-NbO<sub>x</sub> film. a) The high-resolution cross-sectional scanning transmission electron microscopy image of ITO-in-NbO<sub>x</sub>. Reproduced with permission.<sup>[65]</sup> Copyright 2013, Nature Publishing Group. b) Chemical condensation of POM films, [NbO<sub>6</sub>] octahedral and oxygen atoms are shown in green and red, respectively. c) EC performance for a chemically condensed ITO-in-NbO<sub>x</sub> composite film under different applied voltages (half-cell measurements in the liquid electrolyte). The photographs show the visual color change for the composite film on ITO-coated glass when switched from a transparent mode (at 4.0 V, versus Li<sup>+</sup>/Li) to a dark mode (at 1.5 V). d) EC performance for a full solid-state EC device fabricated on PET flexible substrates. The inset photograph in (d) shows a flexible device when bent. Reproduced with permission.<sup>[107]</sup> Copyright 2016, Nature Publishing Group.

a similar system by using LiTaO<sub>3</sub> as an electrolyte instead of Ta<sub>2</sub>O<sub>5</sub>. Li<sup>+</sup> insertion at a low voltage (3 V, cell potential) could induce partial phase change of VO<sub>2</sub> from monoclinic to rutile and reduce its phase change temperature by more than 10 °C, indicating that the TC process can occur at lower temperatures.<sup>[42]</sup> However, the performance of these hybrid windows with TC and EC properties is inferior in terms of both optical contrast and switching speed.

### 3. Organic EC Materials

Despite their inferior thermal resistance and chemical stability compared to inorganic ones, organic materials have been used as key components in EC devices because of their enhanced coloration efficiency,<sup>[112]</sup> high processability, high color versatility, and fast switching speed.<sup>[40]</sup> Viologen is one of the most typical organic EC materials and can modulate the coloration

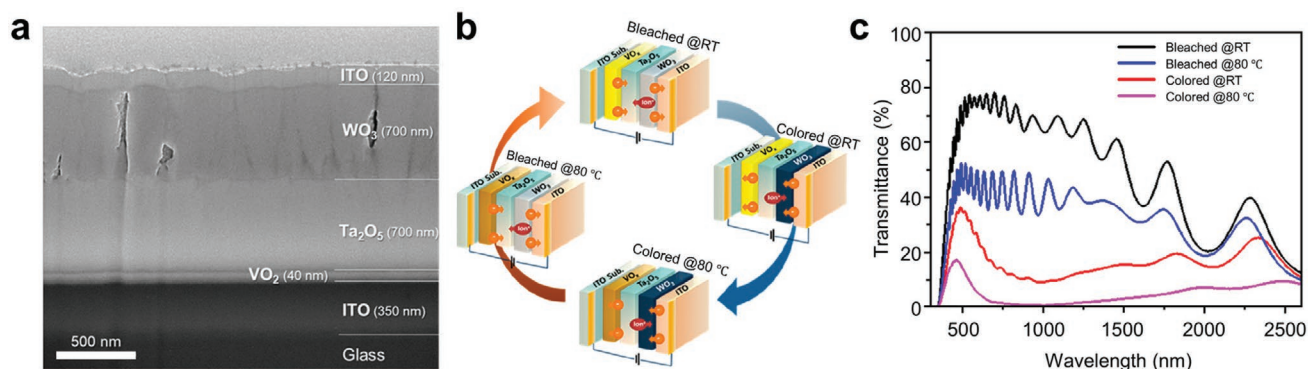


**Figure 15.** Structure, working principle, and EC performance of VO<sub>2</sub>/Ta<sub>2</sub>O<sub>5</sub>/WO<sub>3</sub>-based device. a) Cross-sectional scanning electron microscopy (SEM) image of VO<sub>2</sub>/Ta<sub>2</sub>O<sub>5</sub>/WO<sub>3</sub>-based device. Schematic illustration b) and optical spectra c) of the device at four different optical modes. Reproduced with permission.<sup>[111]</sup> Copyright 2019, American Chemical Society.

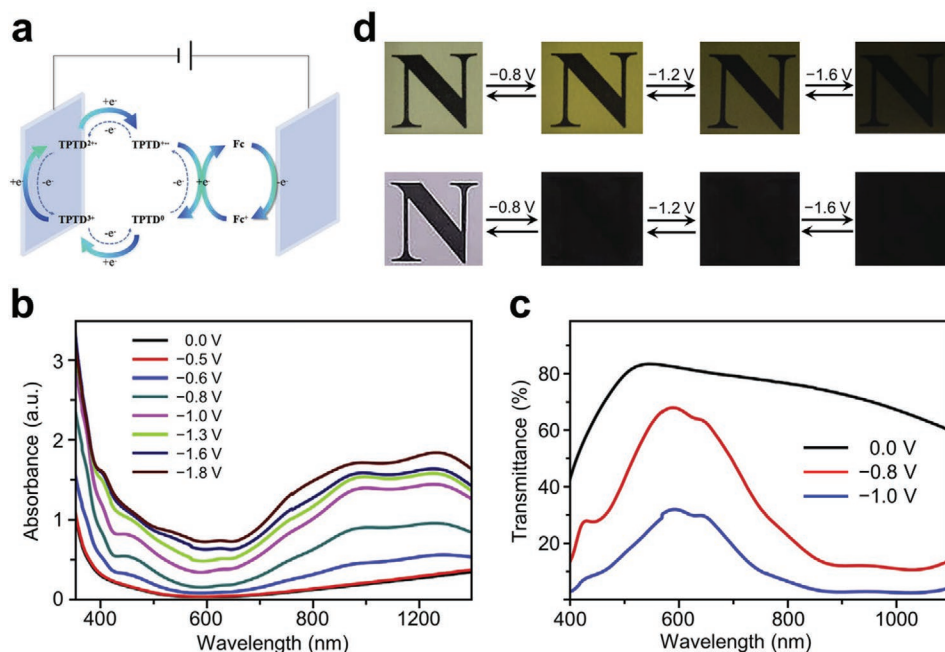


**Figure 16.** Working principle and EC performance of TPTD- and TPPT-based device. a) Diagram for working mechanism of TPTD-based EC device. b) In situ VIS-NIR absorbance response of TPPT-based device at different voltages (versus  $\text{Fc}^+/\text{Fc}$ ). c) Transmission spectra of TPPT-based EC device. d) Corresponding photographs of TPPT-based EC device with a normal camera (upper panel) and NIR camera at 850 nm (lower panel). Reproduced with permission.<sup>[43]</sup> Copyright 2019, Elsevier Ltd.

process through photoelectric charge transfers between N in different valence states on the pyridyl.<sup>[113–114]</sup> Based on this, Wu et al. developed novel dual-band EC devices using 2,4,6-tri(4-pyridyl)-1,3,5-triazine derivatives (TPTD, including 2,4,6-tri(pyridyl-4-propyl)-1,3,5-triazine bromide (TPPT) and 2,4,6-tri(pyridyl-4-benzyl)-1,3,5-triazine bromide (TPBT)). Figure 16a illustrates the working principle of TPTD-based EC devices, which involves the electron transfer between the donator (TPTD species) and the acceptor (ferrocene (Fc)). For example, in TPPT-based EC devices, TPPT switches among different states, including  $\text{TPPT}^{3+}$ ,  $\text{TPPT}^{2+}$ ,  $\text{TPPT}^+$  and  $\text{TPPT}^0$ , at different potentials. The corresponding absorption peaks at 406 and 453 nm (Figure 16b) are ascribed to the formation of  $\text{TPPT}^+$  and  $\text{TPPT}^{2+}$ , respectively. In addition, the device exhibited bright, cool, and dark modes with high modulation contrasts of 50% at 600 nm and 66% at 887 nm (Figure 16c). Accordingly, the device exhibited multiple colors from colorless to yellow to deep olive (upper panel Figure 16d) and different NIR absorption intensities (lower panel in Figure 16d) at various voltages, demonstrating the potential application of organic materials in dual-band EC devices.<sup>[43]</sup> Organic mixed valence compounds are another class of molecules with EC behavior induced by optically induced intervalence charge transfer transitions. Capodilupo et al. fabricated a series of EC devices based on dibenzofulvene derivatives. Their EC behavior can be tuned by various functionalization on the exocyclic fulvene bond of the dibenzofulvene moiety. One of the derivatives, N<sub>2</sub>,N<sub>2</sub>,N<sub>7</sub>,N<sub>7</sub>-Tetrakis(4-methoxyphenyl)-9-(4-methylbenzylidene)-9H-fluorene-2,7-diamine-based device exhibited dual-band EC behavior with fast response time and excellent durability.<sup>[115]</sup> In addition, conducting polymers, such as poly(3,4-ethylenedioxythiophene)

(PEDOT), polythiophenes (PTs), polyaniline (PANI) and its derivatives have also been explored as EC devices.<sup>[116]</sup> PEDOT has been well-known because of its EC behavior in the visible range, but its IR EC property has not been studied. Jonsson et al. presented a PEDOT-based metal-free flexible IR EC device for the first time. PEDOT film exhibits distinct absorption spectra between the reduced and oxidized states in both VIS and NIR regions. At a reduced voltage, PEDOT film turns into the reduced state with an increased absorption at around 600 nm, with a reduced free charge carrier absorption in the IR region.<sup>[117]</sup> Polyaniline (PANI) is another most extensively-studied EC polymers because of its advantages, such as excellent stability and high conductivity.<sup>[118]</sup> Gimeno et al. found that the dual-band EC performance of PEDOT (coloration efficiency, cycle stability, and optical contrast) can be enhanced after being complementary with PANI, however, the detailed reason was not given.<sup>[119]</sup> These reports indicate the potential of organic materials in dual-band EC applications.

#### 4. Hybrid Composite EC Materials

Organic EC materials exhibit high processability, rich color, and fast switching speed, however, they are generally inferior in heat resistance, chemical stability, device durability, and NIR regulation capability. Complementary properties can be found in most inorganic materials, such as outstanding LSPR-caused NIR modulation, enhanced stability, and so on. Therefore, integration of organic and inorganic EC materials into one device can make full use of the advantages of both components to achieve a wide regulation region, rich color, and excellent stability.<sup>[115,120]</sup>



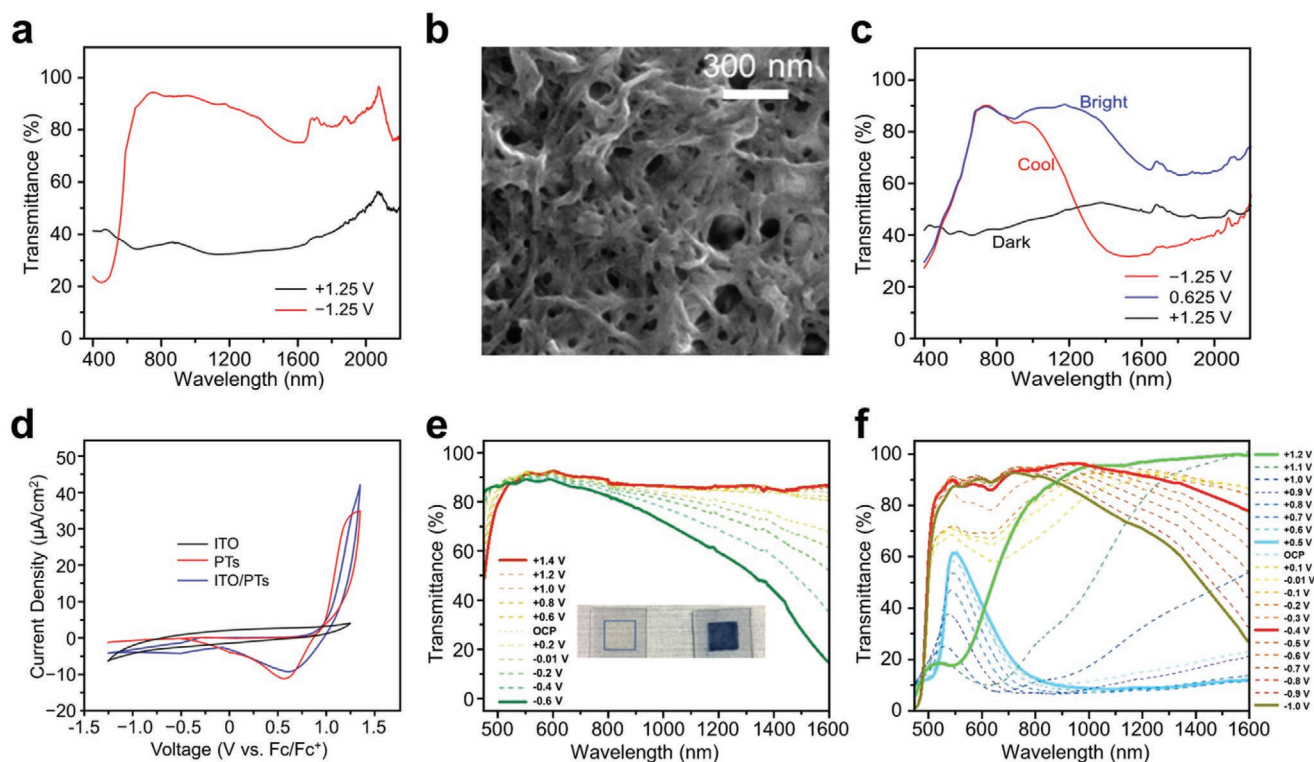


**Figure 17.** Structure and EC performance of the composite EC device. a) Transmission spectra of a PTs film at indicated voltages (versus ferrocenium ion/ferrocene ( $\text{Fc}^+/\text{Fc}$ )). b) SEM image of ITO/PTs composites. c) Transmission spectra of the ITO/PTs film at indicated voltages (versus  $\text{Fc}^+/\text{Fc}$ ). d) CV curves of ITO NPs, PTs, and ITO/PTs films in  $\text{LiClO}_4/\text{PC}$ . Reproduced with permission.<sup>[121]</sup> Copyright 2016, American Chemical Society. Transmission spectra of the nanoporous ITO NC-electrode e) before and f) after electrodeposition of PANI at indicated voltages (versus  $\text{AgCl}/\text{Ag}$ ). The images in insets of (e) are the ITO and PANI/ITO electrodes at OCP. Reproduced with permission.<sup>[127]</sup> Copyright 2020, American Chemical Society.

To this respect, Barile et al. constructed a composite dual-band EC material by integrating PTs and ITO NPs together to regulate VIS and NIR light, respectively.<sup>[121]</sup> At  $-1.25$  V (versus  $\text{Fc}^+/\text{Fc}$ ) the PTs films were high transparency at wavelengths above  $600$  nm in their reduced state and appear yellow in color. On the other hand, under  $1.25$  V, the film absorbed red and NIR light and turned deep blue (Figure 17a). Thus, the as-obtained porous ITO/PTs composite films (Figure 17b) possessed three EC modes including bright, cool, and dark at various voltages with maximum contrasts of 47% and 39% at  $700$  and  $1250$  nm, respectively (Figure 17c). Moreover, CV measurements of ITO/PTs composite film and its components (Figure 17d) were performed to understand its EC mechanism. No faradaic current was obtained on the ITO NC film, indicating that NIR modulation of ITO NPs was a result of capacitive charging. In contrast, the redox of PTs film was observed, corresponding to the modes switching between dark and bright. In addition to the three-state conductivity and corresponding color of each state of PANI,<sup>[122]</sup> the pH of the medium can also trigger the doping of PANI by changing its protonation, resulting in changes in conductivity and optical property.<sup>[123]</sup> This unique feature endows PANI great opportunity to construct hybrid composite EC materials with improved EC behavior than its components.  $\text{WO}_3$  and  $\text{TiO}_2$  have been employed to cooperate with PANI to fabricate organic-inorganic hybrid composite systems with enhanced EC properties such as faster switching speed and improved

stability, which is attributed to the interfacial interaction between PANI and the inorganic components.<sup>[124–125]</sup> Moreover, some dual-band EC devices based on organic-inorganic hybrid composites exhibit a VIS and NIR-selective and independent modulation. Xu et al. constructed a high-performance EC device based on surface-confined  $\text{WO}_3$  and N-methyl-phenothiazine (NMP).  $\text{WO}_3$  is NIR-active with an optical contrast of 85% at  $1000$  nm between  $0$  and  $-1.0$  V (versus Ag wire in  $\text{LiClO}_4/\text{PC}$ ). While NMP delivered an optical contrast of 90% at  $535$  nm in the potential range of  $0$  to  $0.9$  V. The complementary EC properties and compatibility of the two components are responsible for the excellent EC performance of the hybrid composite device.<sup>[126]</sup> More recently, Manca et al. presented an organic-inorganic composite dual-band EC device to achieve four-state modulation by combining the broad NIR response of ITO NCs and high VIS contrast of PANI. Figure 17e,f shows the transmission spectra of ITO NCs and PANI electrodeposited on ITO NCs (ITO/PANI). As shown in Figure 17e, porous ITO NC-electrode itself exhibited an increasing NIR absorption with decreasing potential till  $-0.6$  V (versus  $\text{AgCl}/\text{Ag}$ ) with a maximum contrast of 80% at  $1600$  nm. However, upon electrodeposition of PANI, the ITO/PANI composite delivered a dual-band EC response with much-enhanced contrasts at different voltages due to the complementary regulation regions and distinct potential ranges of PANI and ITO NCs. At positive potentials, ITO NCs were nearly transparent over the VIS

and NIR regions, with the redox state of PANI dominating the EC response in the VIS range. In contrast, at negative bias voltages, most VIS light passed through the reduced PANI, and the transparency degree of NIR light was controlled by the LSPR scattering effect of ITO NCs (Figure 17f). The excellent optical behavior of the composite was ascribed to the high active surface area and the efficient interfacial charge transfer between ITO and PANI.<sup>[127]</sup>

Dual-band modulation effects have also been reported from the hybrid system combining EC and TC properties of organic and inorganic components. Liang et al. presented a novel hybrid system composed of electro-responsive liquid crystals (LCs) micro-domains and thermo-responsive W-VO<sub>2</sub> NCs, which offered four different optical modes under different temperatures and various external voltages. The hybrid film delivered reversible transmittance of VIS light with a contrast from 60.8% to 1.3% at 550 nm by controlling the orientation of the LCs under different voltages. The NIR passage of film can be modulated with contrast from 59.4% to 41.2% at 1150 nm, originating from the TC behavior of W-VO<sub>2</sub> NCs.<sup>[41]</sup>

## 5. Conclusion, Outlook and Future Challenges

The composition of the EC materials (inorganic, organic materials, and composites) and the optical performance of corresponding dual-band EC films/devices are summarized in Table 1. It can be seen that: 1) inorganic materials constitute the majority of dual-band EC materials, especially WO<sub>3</sub>- and TiO<sub>2</sub>-based materials and composites that have been extensively designed and explored, because of their better performance such as higher contrast and much-enhanced stability compared with the organic material-containing ones. 2) WO<sub>3</sub>-based single-component EC films possess a faster coloring than bleaching process, whereas TiO<sub>2</sub>-based ones are reversed, which could be attributed to the distinct crystalline structures of these two materials and their different electrostatic affinities with Li<sup>+</sup>. 3) Metal-doping or O-vacancy introduction is necessary for realizing the dual-band EC behavior of the metal oxides by improving their charge carrier density and reducing the diffusion barrier of Li<sup>+</sup>.<sup>[24,128]</sup> 4) Small particle size and abundant porous structure contribute to improving the EC performance of the device by providing higher surface accessibility and shortening the diffusion paths of intercalation ions.<sup>[52–53,129]</sup> 5) The composition of the electrolyte exerts an important influence on the EC behavior. On the one hand, the nature of intercalation ions, such as ionic radius, valence, and the electrostatic affinity between ions and hosts, plays a key role in improving the switching speed, optical contrast, and stability.<sup>[27,130]</sup> On the other hand, the faradaic current during the efficient redox of the electrolyte can trigger electron injection, thus improving the optical contrast and switching speed.<sup>[25]</sup>

Significant efforts have been devoted to exploring novel dual-band EC materials/composites with excellent EC performance since the pioneering report in 2013. The most recent progress of dual-band EC materials, including inorganic, organic materials, and their composites have been discussed and summarized in this review. Despite the remarkable progress that novel dual-band EC materials have been achieved by optimizing the

structure of EC materials and the composition of electrolytes, there are some critical issues that need to be addressed to boost their future research and widespread implementation. Firstly, the EC performance of the dual-band devices are not satisfied since there is always a trade-off among the optical contrast, switching speed, and cycle stability of the devices. When it comes to the all-solid-state device, poor EC performance such as narrower regulation region, reduced optical contrast, and extended operation potential range are always observed compared with those of the films, which can be attributed to the absorption of the organic electrolyte itself, enhanced electrical resistance, and increased viscosity and the resulting diffusion resistance. Secondly, completely independent control over the VIS and NIR light still remains an unmet key target, as EC devices with selective regulation of VIS light while maintaining high NIR transmittance have been rarely achieved. Moreover, a comprehensive EC test criterion should be proposed to improve the performance and facilitate the comparisons among the devices reported by different research groups, which could in turn shed light on the optimization of the EC materials. For example, in some reports, optical contrast and stability profiles are given in different conditions (usually media), which might be due to the inferior performance in an identical condition. In addition, optical contrast should also be provided in an integral manner<sup>[131]</sup> instead of just contrast values at a few wavelengths. Finally, development of large-area dual-band EC smart windows with excellent performance is highly desired but greatly limited by degraded optical contrast, declining switching speed, and a non-uniform EC process as the device is scaled up.<sup>[19]</sup> Most recently, Manca et al. fabricated a large-area (30 × 30 cm<sup>2</sup>) EC window prototype after balancing the trade-off between the ionic conductivity and the stability in a wide range of temperatures by optimizing the composition of the polymeric gel electrolytes.<sup>[131]</sup>

The following strategies are helpful to improve the performance of the dual-band EC device and to meet real applications (Figure 18). (1) Novel dual-band EC materials with multi-doping, diverse particle sizes,<sup>[53]</sup> low dimensional nanostructures,<sup>[132]</sup> porous property, various morphologies<sup>[29]</sup> and compositions, crystalline structures<sup>[133]</sup> are encouraged to be synthesized, supplemented by different types of electrolytes<sup>[134]</sup> and elaborate in-situ characterizations<sup>[135–137]</sup> to demonstrate high-performance dual-band EC devices with selective and independent optical modulation and improved ion transport rate, and further help to fully understand the mechanism of dual-band EC progress as well. (2) The composition and pattern of the ion-storage layer should be optimized to ensure high optical contrast, accelerate the switching process, and fabricate large-area devices. Meanwhile, the total amount of active ions in ion storage layer is encouraged to be optimized, as the leaching of excess ions could cause the formation of dendrites and bring about degradation of the EC performance. (3) Advanced film forming technologies should be developed to increase the interfacial area between the EC layer and the substrate to facilitate heterogeneous electron transfer and improve the durability of the EC devices. The above-mentioned strategies should be taken into consideration to develop dual-band EC devices with outstanding performance in order to promote their commercialization and build an energy-saving society.

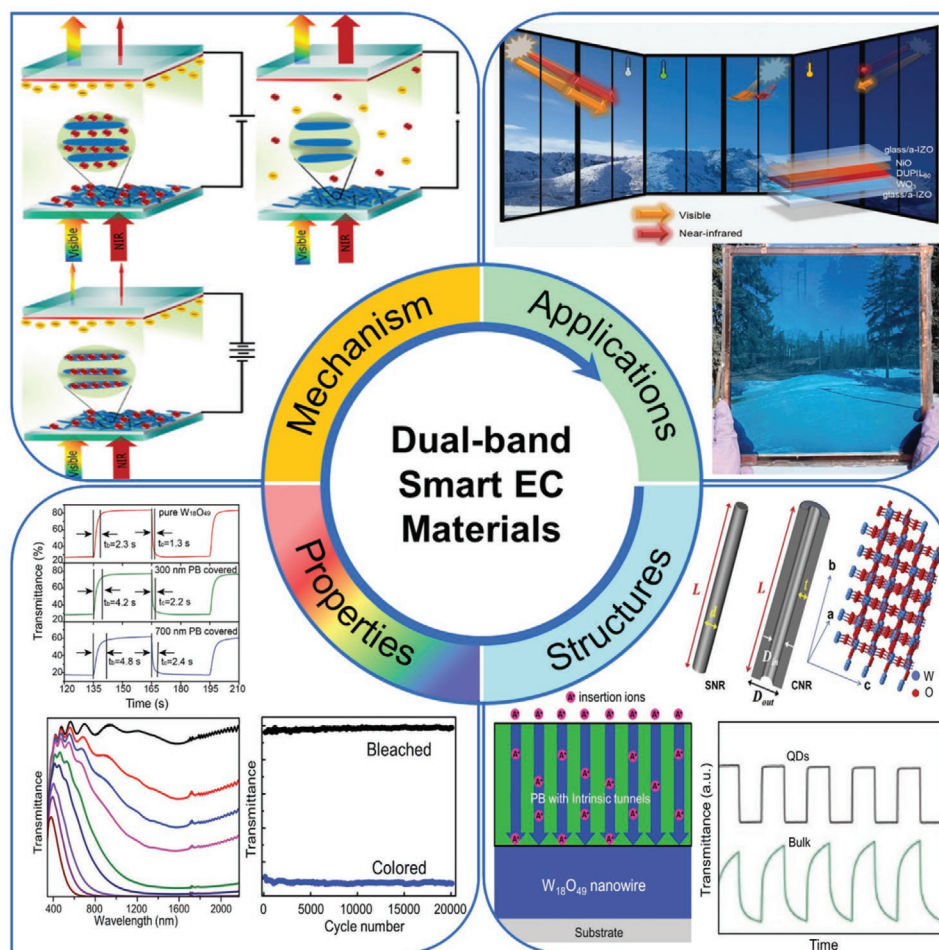


**Figure 18.** The perspectives on the future design, performance improvement, and mechanism investigation in order to promote the application of dual-band smart EC materials. Reproduced with permission.<sup>[19,25,29,46,52–53,83,89]</sup> Copyright 2019, American Chemical Society, Copyright 2016 and 2018, Royal Society of Chemistry. Copyright 2017 and 2020, Elsevier Ltd. Copyright 2014, 2017, and 2020, Wiley-VCH.

## Acknowledgements

Y.Z. acknowledges the support from the National Natural Scientific Foundation of China (21804074) and China Postdoctoral Science Foundation (2020T130331). Z.Z. acknowledges the Open-project of the State Key Laboratory of Physical Chemistry of Solid Surface (Xiamen University) (202023). J.C. acknowledges the Henry Samueli School of Engineering & Applied Science and the Department of Bioengineering at the University of California, Los Angeles for the startup support.

## Conflict of Interest

The authors declare no conflict of interest.

## Keywords

electrochromic devices, energy-saving, independent regulation, near-infrared, smart windows, visible light

Received: September 29, 2021

Revised: December 16, 2021

Published online:

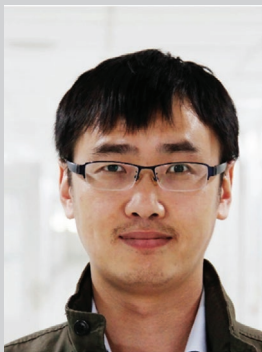
- [1] R. J. Mortimer, *Chem. Soc. Rev.* **1997**, 26, 147.
- [2] C. G. Granqvist, *Handbook of Inorganic Electrochromic Materials*, Elsevier, xxxx **1995**.
- [3] J. R. Platt, *J. Chem. Phys.* **1961**, 34, 862.
- [4] S. K. Deb, *Appl. Opt.* **1969**, 8, 192.
- [5] J. S. E. M. Svensson, C. G. Granqvist, *Sol. Energy Mater.* **1985**, 12, 391.
- [6] C. G. Granqvist, E. Avendaño, A. Azens, *Thin Solid Films* **2003**, 442, 201.
- [7] R. J. Mortimer, A. L. Dyer, J. R. Reynolds, *Displays* **2006**, 27, 2.
- [8] N. Kobayashi, S. Miura, M. Nishimura, H. Urano, *Sol. Energy Mater. Sol. Cells* **2008**, 92, 136.
- [9] W. Weng, T. Higuchi, M. Suzuki, T. Fukuoka, T. Shimomura, M. Ono, L. Radhakrishnan, H. Wang, N. Suzuki, H. Oveis, Y. Yamauchi, *Angew. Chem., Int. Ed.* **2010**, 49, 3956.
- [10] G. Cai, X. Wang, M. Cui, P. Darmawan, J. Wang, A. L.-S. Eh, P. S. Lee, *Nano Energy* **2015**, 12, 258.
- [11] H. Li, J. Li, C. Hou, D. Ho, Q. Zhang, Y. Li, H. Wang, *Adv. Mater. Technol.* **2017**, 2, 1700047.
- [12] Y. Zhai, Z. Zhu, S. Zhou, C. Zhu, S. Dong, *Nanoscale* **2018**, 10, 3089.
- [13] F. J. Berger, T. M. Higgins, M. Rother, A. Graf, Y. Zakharko, S. Allard, M. Matthiesen, J. M. Gotthardt, U. Scherf, J. Zaumseil, *ACS Appl. Mater. Interfaces* **2018**, 10, 11135.

- [14] H. Wang, M. Barrett, B. Duane, J. Gu, F. Zenhausern, *Mater. Sci. Eng., B* **2018**, 228, 167.
- [15] C. Xie, W. Chen, S. Du, D. Yan, Y. Zhang, J. Chen, B. Liu, S. Wang, *Nano Energy* **2020**, 71, 104653.
- [16] J. Sun, Y. Li, J. Sun, Z. Zhu, Y. Zhai, S. Dong, *Chem. Commun.* **2019**, 55, 12060.
- [17] Y. Zhai, Y. Li, Z. Zhu, C. Zhu, D. Du, Y. Lin, *ACS Appl. Mater. Interfaces* **2019**, 11, 48013.
- [18] M. Wu, Y. Shi, R. Li, P. Wang, *ACS Appl. Mater. Interfaces* **2018**, 10, 39819.
- [19] H. Li, W. Zhang, A. Y. Elezzabi, *Adv. Mater.* **2020**, 32, 2003574.
- [20] Y. Zhai, Y. Li, H. Zhang, D. Yu, Z. Zhu, J. Sun, S. Dong, *ACS Appl. Mater. Interfaces* **2019**, 11, 28072.
- [21] Z. Zhu, Y. Zhai, Z. Li, P. Zhu, S. Mao, C. Zhu, D. Du, L. A. Belfiore, J. Tang, Y. Lin, *Mater. Today* **2019**, 30, 52.
- [22] E. L. Runnerstrom, A. Llordés, S. D. Lounis, D. J. Milliron, *Chem. Commun.* **2014**, 50, 10555.
- [23] H. Gu, C. Guo, S. Zhang, L. Bi, T. Li, T. Sun, S. Liu, *ACS Nano* **2018**, 12, 559.
- [24] S. Zhang, S. Cao, T. Zhang, J. Y. Lee, *Adv. Mater.* **2020**, 32, 2004686.
- [25] P. Pattathil, R. Scarfiello, R. Giannuzzi, G. Veramonti, T. Sibillano, A. Quattieri, C. Giannini, P. D. Cozzoli, M. Manca, *Nanoscale* **2016**, 8, 20056.
- [26] S. Zhang, Y. Li, T. Zhang, S. Cao, Q. Yao, H. Lin, H. Ye, A. Fisher, J. Y. Lee, *ACS Appl. Mater. Interfaces* **2019**, 11, 48062.
- [27] S. Zhang, S. Cao, T. Zhang, A. Fisher, J. Y. Lee, *Energy Environ. Sci.* **2018**, 11, 2884.
- [28] S. Cao, S. Zhang, T. Zhang, Q. Yao, J. Y. Lee, *Joule* **2019**, 3, 1152.
- [29] R. Giannuzzi, R. Scarfiello, T. Sibillano, C. Nobile, V. Grillo, C. Giannini, P. D. Cozzoli, M. Manca, *Nano Energy* **2017**, 41, 634.
- [30] Q. Zhao, Y. Fang, K. Qiao, W. Wei, Y. Yao, Y. Gao, *Sol. Energy Mater. Sol. Cells* **2019**, 194, 95.
- [31] G. Cai, J. Wang, P. S. Lee, *Acc. Chem. Res.* **2016**, 49, 1469.
- [32] G. Cai, A. L.-S. Eh, L. Ji, P. S. Lee, *Adv. Sustainable Syst.* **2017**, 1, 1700074.
- [33] Y. Wang, E. L. Runnerstrom, D. J. Milliron, *Annu. Rev. Chem. Biomol. Eng.* **2016**, 7, 283.
- [34] A. Cannavale, P. Cossari, G. E. Eperon, S. Colella, F. Fiorito, G. Gigli, H. J. Snaith, A. Listorti, *Energy Environ. Sci.* **2016**, 9, 2682.
- [35] Z. Tong, Y. Tian, H. Zhang, X. Li, J. Ji, H. Qu, N. Li, J. Zhao, Y. Li, *Sci. China Chem.* **2017**, 60, 13.
- [36] G. Yang, Y.-M. Zhang, Y. Cai, B. Yang, C. Gu, S. X.-A. Zhang, *Chem. Soc. Rev.* **2020**, 49, 8687.
- [37] W. Zhang, H. Li, E. Hopmann, A. Y. Elezzabi, *Nanophotonics* **2021**, 10, 825.
- [38] L. Zhang, H. Wang, J. Liu, Q. Zhang, H. Yan, *J. Mater. Sci.: Mater. Electron.* **2020**, 31, 861.
- [39] K. Wang, Q. Meng, Q. Wang, W. Zhang, J. Guo, S. Cao, A. Y. Elezzabi, W. W. Yu, L. Liu, H. Li, *Adv. Energy Sustainable Res.* **2021**, 2, 2100117.
- [40] Z. Wang, X. Wang, S. Cong, F. Geng, Z. Zhao, *Mater. Sci. Eng., R* **2020**, 140, 100524.
- [41] X. Liang, M. Chen, S. Guo, L. Zhang, F. Li, H. Yang, *ACS Appl. Mater. Interfaces* **2017**, 9, 40810.
- [42] H. Jia, X. Cao, Z. Shao, S. Long, L. Jin, L. Ma, T. Chang, F. Xu, Y. Yang, S. Bao, P. Jin, *Sol. Energy Mater. Sol. Cells* **2019**, 200, 110045.
- [43] N. Wu, L. Ma, S. Zhao, D. Xiao, *Sol. Energy Mater. Sol. Cells* **2019**, 195, 114.
- [44] W. Wu, M. Wang, J. Ma, Y. Cao, Y. Deng, *Adv. Electron Mater.* **2018**, 4, 1800185.
- [45] K. Thummavichai, Y. Xia, Y. Zhu, *Prog. Mater. Sci.* **2017**, 88, 281.
- [46] Z. Wang, Q. Zhang, S. Cong, Z. Chen, J. Zhao, M. Yang, Z. Zheng, S. Zeng, X. Yang, F. Geng, Z. Zhao, *Adv. Opt. Mater.* **2017**, 5, 1700194.
- [47] C. G. Granqvist, *Thin Solid Films* **2014**, 564, 1.
- [48] C. G. Granqvist, M. A. Arvizu, İ. Bayrak Pehlivan, H. Y. Qu, R. T. Wen, G. A. Niklasson, *Electrochim. Acta* **2018**, 259, 1170.
- [49] V. A. Maiorov, *Opt. Spectrosc.* **2019**, 126, 412.
- [50] G. F. Cai, J. P. Tu, D. Zhou, X. L. Wang, C. D. Gu, *Sol. Energy Mater. Sol. Cells* **2014**, 124, 103.
- [51] D. Ma, G. Shi, H. Wang, Q. Zhang, Y. Li, *J. Mater. Chem. A* **2013**, 1, 684.
- [52] S. Cong, Y. Tian, Q. Li, Z. Zhao, F. Geng, *Adv. Mater.* **2014**, 26, 4260.
- [53] Y. Yao, Q. Zhao, W. Wei, Z. Chen, Y. Zhu, P. Zhang, Z. Zhang, Y. Gao, *Nano Energy* **2020**, 68, 104350.
- [54] I. Kriegel, F. Scotognella, L. Manna, *Phys. Rep.* **2017**, 674, 1.
- [55] X. Liu, M. T. Swihart, *Chem. Soc. Rev.* **2014**, 43, 3908.
- [56] Z. Liu, Y. Zhong, I. Shafei, R. Borman, S. Jeong, J. Chen, Y. Losovyj, X. Gao, N. Li, Y. Du, E. Sarnello, T. Li, D. Su, W. Ma, X. Ye, *Nat. Commun.* **2019**, 10, 1394.
- [57] H. Ehrenreich, H. R. Philipp, *Phys. Rev.* **1962**, 128, 1622.
- [58] E. Hutter, J. H. Fendler, *Adv. Mater.* **2004**, 16, 1685.
- [59] Z. Zhu, P. Yuan, S. Li, M. Garai, M. Hong, Q.-H. Xu, *ACS Appl. Bio Mater.* **2018**, 1, 118.
- [60] J. Liu, L. Chu, Z. Yao, S. Mao, Z. Zhu, J. Lee, J. Wang, L. A. Belfiore, J. Tang, *Acta Mater.* **2020**, 188, 599.
- [61] J. M. Luther, P. K. Jain, T. Ewers, A. P. Alivisatos, *Nat. Mater.* **2011**, 10, 361.
- [62] A. Agrawal, R. W. Johns, D. J. Milliron, *Annu. Rev. Mater. Res.* **2017**, 47, 1.
- [63] G. Garcia, R. Buonsanti, E. L. Runnerstrom, R. J. Mendelsberg, A. Llordés, A. Anders, T. J. Richardson, D. J. Milliron, *Nano Lett.* **2011**, 11, 4415.
- [64] J. Kim, G. K. Ong, Y. Wang, G. LeBlanc, T. E. Williams, T. M. Mattox, B. A. Helms, D. J. Milliron, *Nano Lett.* **2015**, 15, 5574.
- [65] A. Llordés, G. Garcia, J. Gazquez, D. J. Milliron, *Nature* **2013**, 500, 323.
- [66] O. Zandi, A. Agrawal, A. B. Shearer, L. C. Reimnitz, C. J. Dahman, C. M. Staller, D. J. Milliron, *Nat. Mater.* **2018**, 17, 710.
- [67] Y. Kim, S. Cha, J.-H. Kim, J.-W. Oh, J.-M. Nam, *Nanoscale* **2021**, 13, 9541.
- [68] Y. Ding, R. Huang, L. Luo, W. Guo, C. Zhu, X.-C. Shen, *Inorg. Chem. Front.* **2021**, 8, 636.
- [69] E. Hopmann, A. Y. Elezzabi, *ACS Appl. Mater. Interfaces* **2020**, 12, 1930.
- [70] K. Tang, Y. Zhang, Y. Shi, J. Cui, X. Shu, Y. Wang, Y. Qin, J. Liu, H. H. Tan, Y. Wu, *Appl. Surf. Sci.* **2019**, 498, 143796.
- [71] L. Shen, J. Zheng, C. Xu, *Nanoscale* **2019**, 11, 23049.
- [72] W. Wang, A. Janotti, C. G. Van de Walle, *J. Mater. Chem. C* **2016**, 4, 6641.
- [73] K. Adachi, T. Asahi, *J. Mater. Res.* **2012**, 27, 965.
- [74] H. Takeda, K. Adachi, *J. Am. Ceram. Soc.* **2007**, 90, 4059.
- [75] K. Manthiram, A. P. Alivisatos, *J. Am. Chem. Soc.* **2012**, 134, 3995.
- [76] Z.-F. Huang, J. Song, L. Pan, X. Zhang, L. Wang, J.-J. Zou, *Adv. Mater.* **2015**, 27, 5309.
- [77] Z. Tong, S. Liu, X. Li, J. Zhao, Y. Li, *Nanoscale Horiz.* **2018**, 3, 261.
- [78] S. Heo, J. Kim, G. K. Ong, D. J. Milliron, *Nano Lett.* **2017**, 17, 5756.
- [79] M.-S. Wu, L.-J. Lyu, J.-H. Syu, *J. Power Sources* **2015**, 297, 75.
- [80] R. Y. Wang, C. D. Wessells, R. A. Huggins, Y. Cui, *Nano Lett.* **2013**, 13, 5748.
- [81] A. Comin, L. Manna, *Chem. Soc. Rev.* **2014**, 43, 3957.
- [82] T. M. Mattox, A. Bergerud, A. Agrawal, D. J. Milliron, *Chem. Mater.* **2014**, 26, 1779.
- [83] M. A. Cardoso, R. F. P. Pereira, S. Pereira, H. Gonçalves, M. M. Silva, L. D. Carlos, S. C. Nunes, E. Fortunato, R. A. S. Ferreira, R. Rego, V. de Zea Bermudez, *Adv. Sustainable Syst.* **2019**, 3, 1800115.
- [84] G. Li, S. Zhang, C. Guo, S. Liu, *Nanoscale* **2016**, 8, 9861.

- [85] C. J. Dahlman, Y. Tan, M. A. Marcus, D. J. Milliron, *J. Am. Chem. Soc.* **2015**, *137*, 9160.
- [86] S. Bogati, A. Georg, C. Jerg, W. Graf, *Sol. Energy Mater. Sol. Cells* **2016**, *157*, 454.
- [87] A. Georg, A. Georg, *Sol. Energy Mater. Sol. Cells* **2009**, *93*, 1329.
- [88] L. Niklaus, M. Schott, U. Posset, G. A. Giffin, *ChemElectroChem* **2020**, *7*, 3274.
- [89] S. Zhang, S. Cao, T. Zhang, Q. Yao, A. Fisher, J. Y. Lee, *Mater. Horiz.* **2018**, *5*, 291.
- [90] M. Ottaviani, S. Panero, S. Morzilli, B. Scrosati, M. Lazzari, *Solid State Ionics* **1986**, *20*, 197.
- [91] N. N. Dinh, N. T. T. Oanh, P. D. Long, M. C. Bernard, A. Hugot-Le Goff, *Thin Solid Films* **2003**, *423*, 70.
- [92] M. Barawi, L. De Trizio, R. Giannuzzi, G. Veramonti, L. Manna, M. Manca, *ACS Nano* **2017**, *11*, 3576.
- [93] M. Barawi, G. Veramonti, M. Epifani, R. Giannuzzi, T. Sibillano, C. Giannini, A. Rougier, M. Manca, *J. Mater. Chem. A* **2018**, *6*, 10201.
- [94] F. De Angelis, C. Di Valentin, S. Fantacci, A. Vittadini, A. Selloni, *Chem. Rev.* **2014**, *114*, 9708.
- [95] B. J. Morgan, G. W. Watson, *Phys. Rev. B* **2010**, *82*, 144119.
- [96] J. H. Richter, A. Henningsson, P. G. Karlsson, M. P. Andersson, P. Uvdal, H. Siegbahn, A. Sandell, *Phys. Rev. B* **2005**, *71*, 235418.
- [97] L. De Trizio, R. Buonsanti, A. M. Schimpf, A. Llordes, D. R. Gamelin, R. Simonutti, D. J. Milliron, *Chem. Mater.* **2013**, *25*, 3383.
- [98] S. Cao, S. Zhang, T. Zhang, A. Fisher, J. Y. Lee, *J. Mater. Chem. C* **2018**, *6*, 4007.
- [99] C. J. Dahlman, A. Agrawal, C. M. Staller, J. Adair, D. J. Milliron, *Chem. Mater.* **2019**, *31*, 502.
- [100] A. Agrawal, S. H. Cho, O. Zandi, S. Ghosh, R. W. Johns, D. J. Milliron, *Chem. Rev.* **2018**, *118*, 3121.
- [101] S. Cao, S. Zhang, T. Zhang, J. Y. Lee, *Chem. Mater.* **2018**, *30*, 4838.
- [102] S. N. Svitashcheva, A. M. Gilinsky, *Appl. Surf. Sci.* **2013**, *281*, 109.
- [103] T. R. Gordon, M. Cargnello, T. Paik, F. Mangolini, R. T. Weber, P. Fornasiero, C. B. Murray, *J. Am. Chem. Soc.* **2012**, *134*, 6751.
- [104] K. Liang, X. Chen, Z. Guo, T. Hou, X. Zhang, Y. Li, *Phys. Chem. Chem. Phys.* **2016**, *18*, 24370.
- [105] Y. Shi, M. Sun, Y. Zhang, J. Cui, Y. Wang, X. Shu, Y. Qin, H. H. Tan, J. Liu, Y. Wu, *Sol. Energy Mater. Sol. Cells* **2020**, *212*, 110579.
- [106] H. Zhou, D. Li, M. Hibino, I. Honma, *Angew. Chem., Int. Ed.* **2005**, *44*, 797.
- [107] A. Llordés, Y. Wang, A. Fernandez-Martinez, P. Xiao, T. Lee, A. Poulain, O. Zandi, C. A. Saez Cabezas, G. Henkelman, D. J. Milliron, *Nat. Mater.* **2016**, *15*, 1267.
- [108] I. Mjejri, A. Rougier, M. Gaudon, *Inorg. Chem.* **2017**, *56*, 1734.
- [109] Y. Cui, Y. Ke, C. Liu, Z. Chen, N. Wang, L. Zhang, Y. Zhou, S. Wang, Y. Gao, Y. Long, *Joule* **2018**, *2*, 1707.
- [110] C. Ji, Z. Wu, L. Lu, X. Wu, J. Wang, X. Liu, H. Zhou, Z. Huang, J. Gou, Y. Jiang, *J. Mater. Chem. C* **2018**, *6*, 6502.
- [111] S. J. Lee, D. S. Choi, S. H. Kang, W. S. Yang, S. Nahm, S. H. Han, T. Kim, *ACS Sustainable Chem. Eng.* **2019**, *7*, 7111.
- [112] G. Sonmez, H. Meng, F. Wudl, *Chem. Mater.* **2004**, *16*, 574.
- [113] M. Pan, Y. Ke, L. Ma, S. Zhao, N. Wu, D. Xiao, *Electrochim. Acta* **2018**, *266*, 395.
- [114] M. Zhu, J. Zeng, H. Li, X. Zhang, P. Liu, *Synth. Met.* **2020**, *270*, 116579.
- [115] G. A. Corrente, E. Fabiano, F. Manni, G. Chidichimo, G. Gigli, A. Beneduci, A.-L. Capodilupo, *Chem. Mater.* **2018**, *30*, 5610.
- [116] G. Gunbas, L. Toppare, *Chem. Commun.* **2012**, *48*, 1083.
- [117] R. Brooke, E. Mittra, S. Sardar, M. Sandberg, A. Sawatdee, M. Berggren, X. Crispin, M. P. Jonsson, *J. Mater. Chem. C* **2017**, *5*, 5824.
- [118] M. Deepa, S. Ahmad, K. N. Sood, J. Alam, S. Ahmad, A. K. Srivastava, *Electrochim. Acta* **2007**, *52*, 7453.
- [119] J. Díaz-Sánchez, P. Roquero, J. M. Hernández-Alcántara, A. Rosas-Aburto, H. Vázquez-Torres, M. Gimeno, *Sol. Energy Mater. Sol. Cells* **2019**, *200*, 109973.
- [120] J. Zeng, Y. Wang, K. Rajan, Z. Xiao, R. U. Rehman Sagar, P. Liu, *Sol. Energy Mater. Sol. Cells* **2021**, *226*, 111070.
- [121] C. J. Barile, D. J. Slotcavage, M. D. McGehee, *Chem. Mater.* **2016**, *28*, 1439.
- [122] W. S. Huang, A. G. MacDiarmid, *Polymer* **1993**, *34*, 1833.
- [123] R. J. Cushman, P. M. McManus, S. C. Yang, *Makromol. Chem., Rapid Commun.* **1987**, *8*, 69.
- [124] H. Wei, X. Yan, S. Wu, Z. Luo, S. Wei, Z. Guo, *J. Phys. Chem. C* **2012**, *116*, 25052.
- [125] H. Lv, Y. Wang, L. Pan, L. Zhang, H. Zhang, L. Shang, H. Qu, N. Li, J. Zhao, Y. Li, *Phys. Chem. Chem. Phys.* **2018**, *20*, 5818.
- [126] D. Weng, M. Li, J. Zheng, C. Xu, *J. Mater. Sci.* **2017**, *52*, 86.
- [127] P. Yilmaz, M. Magni, S. Martinez, R. M. Gonzalez Gil, M. Della Pirriera, M. Manca, *ACS Appl. Energy Mater.* **2020**, *3*, 3779.
- [128] N. Zhang, A. Jalil, D. Wu, S. Chen, Y. Liu, C. Gao, W. Ye, Z. Qi, H. Ju, C. Wang, X. Wu, L. Song, J. Zhu, Y. Xiong, *J. Am. Chem. Soc.* **2018**, *140*, 9434.
- [129] R. Malik, D. Burch, M. Bazant, G. Ceder, *Nano Lett.* **2010**, *10*, 4123.
- [130] H. Li, C. J. Firby, A. Y. Elezzabi, *Joule* **2019**, *3*, 2268.
- [131] A. Cots, S. Dicorato, L. Giovannini, F. Favoino, M. Manca, *Nano Energy* **2021**, *84*, 105894.
- [132] S. Wang, S. Zhao, X. Guo, G. Wang, *Adv. Energy Mater.* **2021**, 2100864, <https://doi.org/10.1002/aenm.202100864>.
- [133] N. Li, Y. Li, G. Sun, Y. Ma, T. Chang, S. Ji, H. Yao, X. Cao, S. Bao, P. Jin, *Chem.-Asian J.* **2017**, *12*, 1709.
- [134] N. Nitta, F. Wu, J. T. Lee, G. Yushin, *Mater. Today* **2015**, *18*, 252.
- [135] Y. Tian, W. Zhang, S. Cong, Y. Zheng, F. Geng, Z. Zhao, *Adv. Funct. Mater.* **2015**, *25*, 5833.
- [136] S. Cong, F. Geng, Z. Zhao, *Adv. Mater.* **2016**, *28*, 10518.
- [137] Y. Zhai, Z. Zhu, C. Zhu, K. Chen, X. Zhang, J. Tang, J. Chen, *Mater. Today* **2020**, *38*, 99.



**Yanling Zhai** received her Ph.D. degree in 2015 from Changchun Institute of Applied Chemistry under the supervision of Prof. Shaojun Dong. She then moved to Worcester Polytechnic Institute and Northeastern University for her postdoctoral training and is now a professor at Qingdao University. She has published over 30 papers with a current h-index of 22. Her research interests mainly focus on spectroelectrochemistry and nanomaterial-based catalysis.



**Zhijun Zhu** is currently an associate professor at Qingdao University. He earned his Ph.D. degree in 2014 from Changchun Institute of Applied Chemistry with Prof. Zhenxin Wang. Then, he did his postdoctoral training with Prof. Qing-Hua Xu at the National University of Singapore, Prof. Susan Zhou at the Worcester Polytechnic Institute, and Prof. Ming Su at Northeastern University before joining Qingdao University as a faculty. His research interests include nanomaterial-based electrochromic and catalytic applications.



**Xiaoquan Lu** received his Ph.D. degree from Sun Yat-sen University in 1997. He has been a professor in the College of Chemistry & Chemical Engineering, Northwest Normal University, in 2001, where he is the director of the Key Laboratory of Bioelectrochemistry & Environmental Analysis of Gansu, China. He has been the Cheung Kong Professor of the Ministry of Education (China) since 2013. His current research interests focus on bioelectrochemistry, visual sensing, and new energy technology development.



**Jun Chen** is currently an assistant professor in the Department of Bioengineering at the University of California, Los Angeles. His research focuses on nanotechnology and bioelectronics. With a current h-index of 80, he has published 2 books; 1 book chapter; and 210 journal articles, 120 of them being a corresponding author in Chemical Reviews, Chemical Society Reviews, Nature Materials, Nature Electronics, Nature Communications, Science Advances, Joule, Matter, etc. Among his many accolades are the Materials Thought Leaders by Azom, UCLA Society of Hellman Fellows Award, Okawa Foundation Research Award, Advanced Materials Rising Star, Materials Today Rising Star Award, ACS Nano Rising Stars Lectureship Award, Chem. Soc. Rev. Emerging Investigator Award, Highly Cited Researchers 2019-2021, and many others. Beyond research, he is an associate editor of Biosensors and Bioelectronics.